

Hybrid High-Order formulations with turbulence modelling capabilities for incompressible flow problems

Lorenzo Botti¹, Daniele A. Di Pietro², and Francesco Carlo Massa³

¹Department of Engineering and Applied Sciences, University of Bergamo, Italy, lorenzo.botti@unibg.it

²IMAG, Univ Montpellier, CNRS, Montpellier, France, daniele.di-pietro@umontpellier.fr

³Department of Engineering and Applied Sciences, University of Bergamo, Italy, francescocarlo.massa@unibg.it

June 11, 2025

Abstract

We propose a Hybrid High-Order (HHO) formulation of the incompressible Navier–Stokes equations, that is well suited to be employed for the simulation of turbulent flows. The spatial discretization relies on hybrid velocity and pressure spaces and the temporal discretization is based on Explicit Singly Diagonal Implicit Runge-Kutta (ESDIRK) methods. The formulation possesses some attractive features that can be fruitfully exploited when high-fidelity computations are required, namely: pressure-robustness, conservation of mass enforced cell-by-cell up to machine precision, robustness in the inviscid limit, implicit high-order accurate time stepping with local time step adaptation, reduced memory footprint thanks to static condensation of both velocity and pressure, possibility to exploit inherited p -multilevel solution strategies to improve performance of iterative solvers. After demonstrating the relevant properties of the scheme in practice, performing challenging 2D and 3D test cases, we consider the simulation of the Taylor–Green Vortex flow problem at Reynolds 1 600.

1 Introduction

In recent years, the introduction of Hybrid High-Order (HHO) and Hybridizable Discontinuous Galerkin (HDG) methods has provided a new ground to pursue the development of high-order accurate computational modelling tools for the simulation of incompressible turbulent flows. In contrast to Discontinuous Galerkin methods, HHO and HDG methods are based on degrees of freedom that are broken polynomials on both the mesh and its skeleton. Relevant features of hybrid schemes are: i) local (cell-by-cell) conservation of physical quantities, ii) increased convergence rates in the diffusion-dominated regime (see [14, 16] for a discussion on this subject as well as a comparison between HHO and HDG), iii) robustness with mesh distortion and grading, iv) implicit time integration with reduced memory footprint of the Jacobian matrix.

This work contains a numerical investigation of the HHO scheme of [10] applied to turbulent flows. Unlike previous HHO schemes for incompressible flows (see, e.g., [1, 17, 18, 8]), the one considered relies on a hybrid discretization of both the velocity and pressure. This choice, combined with an appropriate selection of local polynomial spaces, has been shown to be pressure-robust [9] and, provided a suitable discretization of the time derivative and convective stabilization are adopted, Reynolds semi-robust [4]. Following [30], pressure-robustness expresses the fact that the irrotational part of body forces only affects the pressure, leaving the velocity unaltered. Pressure-robust HDG methods with hybrid pressure have been proposed in [34, 26]; see [9, Remark 15] and [4, Remark 8] for a comparison with the method considered here or closely-related variations thereof. Various strategies to obtain pressure-robustness and, possibly, Reynolds-semi-robustness in the framework of HHO methods have been studied in [12, 13, 33], where the case of general polytopal meshes is also considered. The aforementioned articles share in common the idea to reconstruct an $\mathbf{H}(\text{div})$ -conforming velocity approximation starting from non-conforming polynomial spaces. Other research efforts to achieve pressure robustness based on $\mathbf{H}(\text{div})$ -conforming spaces for the velocity have been made in [29, 32].

In order to treat time-dependent problems in the convection-dominated flow regime, we combine here the upwind-stabilized variant of the space discretization of [10] with high-order ESDIRK time integration schemes. Efficient resolution of the algebraic problems relies on p -multigrid preconditioners in the spirit of [7] and on a distributed memory implementation that is well suited to exploit modern HPC facilities. Numerical validation of the approach is carried out using classical two- and three-dimensional test cases. Convergence rates are numerically evaluated for a wide range of Reynolds numbers, encompassing both the viscosity-dominated and convection-dominated regimes. The behaviour of the discretization error is studied for the two-dimensional travelling waves and the three-dimensional Ethier–Steinman [19] solutions. Robustness in the inviscid limit and numerical dissipation are assessed using the double shear layer problem. Pressure-robustness is checked using the solution proposed in [28]. Finally, the capabilities of the proposed ESDIRK-HHO solution strategy are

investigated targeting under-resolved turbulence modelling considering the Taylor–Green vortex problem [37] at Reynolds 1 600.

The paper is organized as follows. In Sections 2 and 3 we respectively present the model problem and its discrete formulation. A comprehensive numerical validation of the method is performed in Section 4 and an application to turbulence modelling is considered in Section 5. Finally, some conclusions are drawn in Section 6.

2 Continuous setting

Given a polygonal or polyhedral domain $\Omega \subset \mathbb{R}^d$, $d \in \{2, 3\}$, with boundary $\partial\Omega$, the initial divergence-free velocity field $\mathbf{u}_0 : \Omega \rightarrow \mathbb{R}^d$, and a finite time t_F , the incompressible Navier–Stokes problem consists in finding the velocity field $\mathbf{u} : \Omega \times [0, t_F] \rightarrow \mathbb{R}^d$, and the pressure field $p : \Omega \times (0, t_F] \rightarrow \mathbb{R}$, such that $\mathbf{u}(\cdot, 0) = \mathbf{u}_0$ and

$$\frac{\partial \mathbf{u}}{\partial t} + \nabla \cdot [(\mathbf{u} \otimes \mathbf{u}) - \nu \nabla \mathbf{u}] + \nabla p = \mathbf{f} \quad \text{in } \Omega \times (0, t_F], \quad (1a)$$

$$\nabla \cdot \mathbf{u} = 0 \quad \text{in } \Omega \times (0, t_F], \quad (1b)$$

$$\mathbf{u} = \mathbf{g}_D \quad \text{on } \partial\Omega_D \times (0, t_F]. \quad (1c)$$

$$p\mathbf{n} - \nu(\nabla \mathbf{u})\mathbf{n} = \mathbf{g}_N \quad \text{on } \partial\Omega_N \times (0, t_F], \quad (1d)$$

where \mathbf{n} denotes the unit vector normal to $\partial\Omega$ pointing out of Ω , $\nu > 0$ is the (constant) viscosity, \mathbf{g}_D and \mathbf{g}_N denote, respectively, the prescribed velocity on the Dirichlet boundary $\partial\Omega_D \subset \partial\Omega$ and the prescribed traction on the Neumann boundary $\partial\Omega_N := \partial\Omega \setminus \partial\Omega_D$, while $\mathbf{f} : \Omega \rightarrow \mathbb{R}^d$ is a given body force.

3 ESDIRK-HHO discretization

3.1 Mesh

We consider meshes of the domain Ω corresponding to couples $\mathcal{M}_h := (\mathcal{T}_h, \mathcal{F}_h)$, where \mathcal{T}_h is a finite collection of polygonal (if $d = 2$) or polyhedral (if $d = 3$) cells such that $h := \max_{T \in \mathcal{T}_h} h_T > 0$ with h_T denoting the diameter of T , while \mathcal{F}_h is a finite collection of polygons (if $d = 2$) or line segments (if $d = 3$) with h_F denoting the diameter of F . It is assumed henceforth that the mesh \mathcal{M}_h is shape- and contact-regular, as detailed in [15, Definition 1.4] and that its trace on $\partial\Omega$ is compatible with the partition $\partial\Omega = \partial\Omega_D \sqcup \partial\Omega_N$. We respectively denote by \mathcal{F}_h^D and \mathcal{F}_h^N the sets of Dirichlet and Neumann faces. For each mesh cell $T \in \mathcal{T}_h$, the faces contained in the cell boundary ∂T are collected in the set \mathcal{F}_T and we additionally let $\partial T^\bullet := \partial T \cap \partial\Omega_\bullet$ for $\bullet \in \{D, N\}$. For all $T \in \mathcal{T}_h$ and all $F \in \mathcal{F}_T$, \mathbf{n}_{TF} denotes the unit vector normal to F pointing out of T and $\mathbf{n}_{\partial T} : \partial T \rightarrow \mathbb{R}^d$ is such that $\mathbf{n}_{\partial T}|_F := \mathbf{n}_{TF}$ for all $F \in \mathcal{F}_T$.

3.2 Discrete spaces

Hybrid High-Order methods hinge on local polynomial spaces on mesh cells and faces. For given integers $\ell \geq 0$ and $n \geq 1$, we denote by \mathbb{P}_n^ℓ the space of n -variate polynomials of total degree $\leq \ell$ (in short, of degree ℓ). For X mesh cell or face, we denote by $\mathcal{P}^\ell(X)$ the space spanned by the restriction to X of functions in \mathbb{P}_d^ℓ .

The global discrete spaces for the velocity and pressure unknowns are respectively defined as follows:

$$\underline{\mathbf{V}}_h^k := \left\{ \underline{\mathbf{v}}_h = ((\mathbf{v}_T)_{T \in \mathcal{T}_h}, (\mathbf{v}_F)_{F \in \mathcal{F}_h}) : \begin{array}{l} \mathbf{v}_T \in \mathcal{P}^{k+1}(T)^d \text{ for all } T \in \mathcal{T}_h, \\ \mathbf{v}_F \in \mathcal{P}^k(F)^d \text{ for all } F \in \mathcal{F}_h \setminus \mathcal{F}_h^N, \\ \mathbf{v}_F \in \mathcal{P}^{k+1}(F)^d \text{ for all } F \in \mathcal{F}_h^N \end{array} \right\}.$$

$$\underline{Q}_h^{k+1} := \left\{ \underline{q}_h = ((q_T)_{T \in \mathcal{T}_h}, (q_F)_{F \in \mathcal{F}_h}) : q_T \in \mathcal{P}^k(T) \text{ for all } T \in \mathcal{T}_h \text{ and } q_F \in \mathcal{P}^{k+1}(F) \text{ for all } F \in \mathcal{F}_h \right\}.$$

The restriction of these spaces and their elements to a mesh cell $T \in \mathcal{T}_h$ are denoted replacing the subscript h by T and are obtained collecting the components attached to T and its boundary. Given $\underline{\mathbf{v}}_T \in \underline{\mathbf{V}}_T^k$, we will also denote by $\mathbf{v}_{\partial T}$ the function such that $\mathbf{v}_{\partial T}|_F = \mathbf{v}_F$ for all $F \in \mathcal{F}_T$. Given $\underline{q}_T \in \underline{Q}_T^{k+1}$, the notation $q_{\partial T}$ is defined similarly.

3.3 Gradient reconstruction operators

For each mesh cell $T \in \mathcal{T}_h$, the tensor and vector gradient reconstruction operators $\mathcal{G}_T^k : \underline{\mathbf{V}}_T^k \rightarrow \mathcal{P}^k(T)^{d \times d}$ and $\mathbf{g}_T^{k+1} : \underline{Q}_T^{k+1} \rightarrow \mathcal{P}^{k+1}(T)^d$ are respectively defined as follows: For all $(\underline{\mathbf{v}}_T, \underline{q}_T) \in \underline{\mathbf{V}}_T^k \times \underline{Q}_T^{k+1}$,

$$\begin{aligned} \int_T \mathcal{G}_T^k \underline{\mathbf{v}}_T : \boldsymbol{\tau} &= \int_T \nabla \mathbf{v}_T : \boldsymbol{\tau} - \int_{\partial T} (\mathbf{v}_T - \mathbf{v}_{\partial T}) \otimes \mathbf{n}_{\partial T} : \boldsymbol{\tau} \quad \forall \boldsymbol{\tau} \in \mathcal{P}^k(T)^{d \times d}, \\ \int_T \mathbf{g}_T^{k+1} \underline{q}_T \cdot \mathbf{v} &= - \int_T q_T \nabla \cdot \mathbf{v} + \int_{\partial T} q_{\partial T} \mathbf{v} \cdot \mathbf{n}_{\partial T} \quad \forall \mathbf{v} \in \mathcal{P}^{k+1}(T)^d. \end{aligned}$$

3.4 Semi-discrete HHO formulation

We first present the semi-discrete formulation of the incompressible Navier–Stokes problem in (1) omitting the terms that are responsible of the imposition of boundary conditions. We remark that the resulting formulation is well suited to tackle the imposition of periodic boundary conditions on $\partial\Omega$, since, in this case, $\mathcal{F}_h^D = \mathcal{F}_h^N = \emptyset$, all faces are internal. The application to periodic computational domains will be often encountered in the test cases proposed in the numerical results section. Notice that a proper handling of internal faces laying on periodic boundaries must be ensured. For example, once periodic boundaries couples are defined, assuming that their faces are properly matched, periodic faces couples can be identified and each pair of faces can be treated as a unique internal face.

Given $(\underline{\mathbf{u}}_T, \underline{p}_T) \in \underline{\mathbf{V}}_T^k \times \underline{Q}_T^{k+1}$, the local spatial discretizations $sd_{T,\text{pBC}}^{\text{slm}}((\underline{\mathbf{u}}_T, \underline{p}_T); \cdot) : \underline{\mathbf{V}}_T^k \rightarrow \mathbb{R}$ of the steady momentum equation and $sd_{T,\text{pBC}}^{\text{cnt}}(\underline{\mathbf{u}}_T; \cdot) : \underline{Q}_T^{k+1} \rightarrow \mathbb{R}$ of the continuity equations for periodic boundary conditions are such that, for all $\underline{\mathbf{v}}_T \in \underline{\mathbf{V}}_T^k$ and all $\underline{q}_T \in \underline{Q}_T^{k+1}$,

$$\begin{aligned} sd_{T,\text{pBC}}^{\text{slm}}((\underline{\mathbf{u}}_T, \underline{p}_T); \underline{\mathbf{v}}_T) &:= - \int_T (\underline{\mathbf{u}}_T \otimes \underline{\mathbf{u}}_T) : \nabla \underline{\mathbf{v}}_T + \int_{\partial T} \left[(\underline{\mathbf{u}}_T \cdot \underline{\mathbf{n}}_{\partial T})^\oplus \underline{\mathbf{u}}_T + (\underline{\mathbf{u}}_T \cdot \underline{\mathbf{n}}_{\partial T})^\ominus \underline{\mathbf{u}}_{\partial T} \right] \cdot (\underline{\mathbf{v}}_T - \underline{\mathbf{v}}_{\partial T}) \\ &\quad + \int_T \nu \mathcal{G}_T^k \underline{\mathbf{u}}_T : \mathcal{G}_T^k \underline{\mathbf{v}}_T + \int_{\partial T} \frac{\nu}{h_T} \boldsymbol{\pi}_{\partial T}^k (\underline{\mathbf{u}}_T - \underline{\mathbf{u}}_{\partial T}) \cdot \boldsymbol{\pi}_{\partial T}^k (\underline{\mathbf{v}}_T - \underline{\mathbf{v}}_{\partial T}) \\ &\quad + \int_T \mathbf{g}_T^{k+1} \underline{p}_T \cdot \underline{\mathbf{v}}_T - \int_T \mathbf{f} \cdot \underline{\mathbf{v}}_T, \\ sd_{T,\text{pBC}}^{\text{cnt}}(\underline{\mathbf{u}}_T; \underline{q}_T) &:= \int_T \mathbf{g}_T^{k+1} \underline{q}_T \cdot \underline{\mathbf{u}}_T, \end{aligned}$$

where $\alpha^\oplus := \frac{1}{2}(\alpha + |\alpha|)$ and $\alpha^\ominus := \frac{1}{2}(\alpha - |\alpha|)$ and $\boldsymbol{\pi}_{\partial T}^k$ is the L^2 -orthogonal projector onto the broken polynomial space $\{\underline{\mathbf{v}} \in L^2(\partial T)^d : \underline{\mathbf{v}}|_F \in \mathcal{P}^k(F)^d \text{ for all } F \in \mathcal{F}_T\}$.

For Dirichlet and Neumann boundary conditions, on the other hand, given $(\underline{\mathbf{u}}_T, \underline{p}_T) \in \underline{\mathbf{V}}_T^k \times \underline{Q}_T^{k+1}$, the local spatial discretizations $sd_T^{\text{slm}}((\underline{\mathbf{u}}_T, \underline{p}_T); \cdot) : \underline{\mathbf{V}}_T^k \rightarrow \mathbb{R}$ of the steady linear momentum and $sd_T^{\text{cnt}}(\underline{\mathbf{u}}_T; \cdot) : \underline{Q}_T^{k+1} \rightarrow \mathbb{R}$ of the continuity equations are respectively such that, for all $\underline{\mathbf{v}}_T \in \underline{\mathbf{V}}_T^k$ and all $\underline{q}_T \in \underline{Q}_T^{k+1}$,

$$\begin{aligned} sd_T^{\text{slm}}((\underline{\mathbf{u}}_T, \underline{p}_T); \underline{\mathbf{v}}_T) &:= sd_{T,\text{pBC}}^{\text{slm}}((\underline{\mathbf{u}}_T, \underline{p}_T); \underline{\mathbf{v}}_T) + \int_{\partial T^N} (\underline{\mathbf{u}}_{\partial T} \cdot \underline{\mathbf{n}}_{\partial T}) (\underline{\mathbf{u}}_{\partial T} \cdot \underline{\mathbf{v}}_{\partial T}) - \int_{\partial T^N} p_{\partial T} (\underline{\mathbf{v}}_{\partial T} \cdot \underline{\mathbf{n}}_{\partial T}) + \int_{\partial T^N} \mathbf{g}_N \cdot \underline{\mathbf{v}}_{\partial T} \quad (2) \end{aligned}$$

$$+ \int_{\partial T^D} (\underline{\mathbf{u}}_{\partial T} \cdot \underline{\mathbf{n}}_{\partial T})^\oplus (\underline{\mathbf{u}}_{\partial T} \cdot \underline{\mathbf{v}}_{\partial T}) + \int_{\partial T^D} (\mathbf{g}_D \cdot \underline{\mathbf{n}}_{\partial T})^\ominus (\mathbf{g}_D \cdot \underline{\mathbf{v}}_{\partial T}) \quad (3)$$

$$+ \int_{\partial T^D} ((\underline{\mathbf{u}}_{\partial T} - \mathbf{g}_D) \otimes \underline{\mathbf{n}}_{\partial T}) : \left(\nu \mathcal{G}_T \underline{\mathbf{v}}_T + \frac{\nu}{h_F} \underline{\mathbf{v}}_{\partial T} \otimes \underline{\mathbf{n}}_{\partial T} \right) - \int_{\partial T^D} \nu \mathcal{G}_T \underline{\mathbf{u}}_T : (\underline{\mathbf{v}}_{\partial T} \otimes \underline{\mathbf{n}}_{\partial T}), \quad (4)$$

$$sd_T^{\text{cnt}}(\underline{\mathbf{u}}_T; \underline{q}_T) := sd_{T,\text{pBC}}^{\text{cnt}}(\underline{\mathbf{u}}_T; \underline{q}_T) - \int_{\partial T^D} (\mathbf{g}_D \cdot \underline{\mathbf{n}}_{\partial T}) \underline{q}_{\partial T} - \int_{\partial T^N} (\underline{\mathbf{u}}_{\partial T} \cdot \underline{\mathbf{n}}_{\partial T}) \underline{q}_{\partial T}.$$

The terms in (3) and (4) are responsible for the weak imposition of Dirichlet boundary conditions and pertain to the spatial discretization of the convective term and the viscous term, respectively, see [8, Remark 6]. The terms in (2) are responsible for the imposition of Neumann boundary conditions: the first and the second term, respectively, pertain to the spatial discretization of the convective term and the pressure gradient.

Given $(\underline{\mathbf{u}}_T, \underline{p}_T) \in \underline{\mathbf{V}}_T^k \times \underline{Q}_T^{k+1}$, the local spatial discretization of the unsteady momentum equation is such that, for all $\underline{\mathbf{v}}_T \in \underline{\mathbf{V}}_T^k$,

$$sd_T^{\text{mnt}}((\underline{\mathbf{u}}_T, \underline{p}_T); \underline{\mathbf{v}}_T) := \int_T \frac{\partial \underline{\mathbf{u}}_T}{\partial t} \cdot \underline{\mathbf{v}}_T + sd_T^{\text{slm}}((\underline{\mathbf{u}}_T, \underline{p}_T); \underline{\mathbf{v}}_T).$$

The global residuals of the spatial discretization $r_h^{\text{mnt}}((\underline{\mathbf{u}}_h, \underline{p}_h); \cdot) : \underline{\mathbf{V}}_h^k \rightarrow \mathbb{R}$ and $r_h^{\text{cnt}}(\underline{\mathbf{u}}_h; \cdot) : \underline{Q}_h^{k+1} \rightarrow \mathbb{R}$ are obtained by cell-by-cell assembly of the local discretizations, *i.e.*: For all $\underline{\mathbf{v}}_h \in \underline{\mathbf{V}}_h^k$ and all $\underline{q}_h \in \underline{Q}_h^{k+1}$,

$$r_h^{\text{mnt}}((\underline{\mathbf{u}}_h, \underline{p}_h); \underline{\mathbf{v}}_h) := \sum_{T \in \mathcal{T}_h} sd_T^{\text{mnt}}((\underline{\mathbf{u}}_T, \underline{p}_T); \underline{\mathbf{v}}_T), \quad r_h^{\text{cnt}}(\underline{\mathbf{u}}_h; \underline{q}_h) := \sum_{T \in \mathcal{T}_h} sd_T^{\text{cnt}}(\underline{\mathbf{u}}_T; \underline{q}_T). \quad (5)$$

The global problem reads: Find $(\underline{\mathbf{u}}_h, \underline{p}_h) \in \underline{\mathbf{V}}_h^k \times \underline{Q}_h^{k+1}$ such that

$$\begin{aligned} r_h^{\text{mnt}}((\underline{\mathbf{u}}_h, \underline{p}_h); \underline{\mathbf{v}}_h) &= 0 & \forall \underline{\mathbf{v}}_h \in \underline{\mathbf{V}}_h^k, \\ r_h^{\text{cnt}}(\underline{\mathbf{u}}_h; \underline{q}_h) &= 0 & \forall \underline{q}_h \in \underline{Q}_h^{k+1}. \end{aligned} \quad (6)$$

3.5 ESDIRK temporal discretization

We describe hereafter the time stepping algorithm focusing, for the sake of simplicity, on the case of periodic boundary conditions. Based on multistage ESDIRK time marching strategies, the solutions $\mathbf{u}_h|_{t+\delta t}, p_h|_{t+\delta t}$ are computed considering an approximated time integration formula for the global residuals in (5) over the time interval δt :

$$\sum_{T \in \mathcal{T}_h} \int_T \frac{\mathbf{u}_T|_{t+\delta t} - \mathbf{u}_T|_t}{\delta t} \cdot \mathbf{v}_T + \sum_{T \in \mathcal{T}_h} \sum_{i=1}^s b_i sd_T^{\text{slm}} \left((\mathbf{u}_T|_{t+\delta t_i}, p_T|_{t+\delta t_i}); \mathbf{v}_T \right) = 0, \quad (7)$$

$$\sum_{T \in \mathcal{T}_h} \sum_{i=1}^s b_i sd_T^{\text{cnt}}(\mathbf{u}_T|_{t+\delta t_i}; q_T) = 0,$$

where, for all $T \in \mathcal{T}_h$, $\mathbf{u}_T|_{t+\delta t_i}$ and $p_T|_{t+\delta t_i}$ are the solutions of the ESDIRK i th-stage, with $\delta t_i = \delta t \sum_{j=1}^i a_{ij}$. The number of stages s and the real coefficients a_{ij} , with $i = 1, \dots, s$ and $j = 1, \dots, i$, uniquely define an ESDIRK formulation. In particular, for all schemes belonging to the ESDIRK family, it holds that $a_{11} = 0$ and $b_i = a_{si}$, for $i = 1, \dots, s$. As a consequence, since $\delta t_1 = 0$ and $\delta t_s = \delta t$, the approximated time integration formula in (7) is equivalent to the last ESDIRK stage and $\mathbf{u}_h|_{t+\delta t}, p_h|_{t+\delta t}$ is the last stage solution. The stages solution are built incrementally, starting from the first stage, moving to second, and so on up to the last stage. In this work we rely on third, fourth and fifth order accurate ESDIRK schemes requiring four, six and eight stages, respectively, see [24, 25] for details. To complete the presentation of the time marching strategy we need to specify how the stages solutions are computed.

Let's introduce the ESDIRK i th-stage formulation. Given $(\mathbf{u}_T|_{t+\delta t_j}, p_T|_{t+\delta t_j}) \in \mathbf{V}_T^k \times Q_T^{k+1}$, with $j = 1, \dots, i$, the local spatial and temporal discretizations $sd_{i,T}^{\text{slm}}((\mathbf{u}_T(t), p_T(t)); \cdot) : \mathbf{V}_T^k \rightarrow \mathbb{R}$ of the momentum equation and $sd_{i,T}^{\text{cnt}}(\mathbf{u}_T(t); \cdot) : Q_T^{k+1} \rightarrow \mathbb{R}$ of the continuity equations at the i th-stage are such that, for all $\mathbf{v}_T \in \mathbf{V}_T^k$ and all $q_T \in Q_T^{k+1}$,

$$std_{i,T}^{\text{mnt}} \left((\mathbf{u}_T(t), p_T(t)); \mathbf{v}_T \right) := \int_T \frac{\mathbf{u}_T|_{t+\delta t_i} - \mathbf{u}_T|_t}{\delta t} \cdot \mathbf{v}_T + \sum_{j=1}^i a_{ij} sd_T^{\text{slm}} \left((\mathbf{u}_T|_{t+\delta t_j}, p_T|_{t+\delta t_j}); \mathbf{v}_T \right) \quad (8a)$$

$$std_{i,T}^{\text{cnt}}(\mathbf{u}_T(t); q_T) := \sum_{j=1}^i a_{ij} sd_T^{\text{cnt}}(\mathbf{u}_T|_{t+\delta t_j}; q_T) \quad (8b)$$

We remark that, the spatial and temporal discretizations $std^{\text{mnt}}(\cdot, \cdot), std^{\text{cnt}}(\cdot, \cdot)$ defined in (7)-(8) are formulated omitting the dependence from the boundary conditions and forcing terms. In doing so, we implicitly assume that \mathbf{f} (and also $\mathbf{g}_N, \mathbf{g}_D$ when non-periodic boundary conditions are considered) is evaluated at the same time points as the velocity and pressure variables \mathbf{u}_T, p_T .

The global residuals of the ESDIRK i th-stage $r_{i,h}^{\text{mnt}} \left((\mathbf{u}_h(t), p_h(t)); \cdot \right) : \mathbf{V}_h^k \rightarrow \mathbb{R}$, and $r_{i,h}^{\text{cnt}}(\mathbf{u}_h(t); \cdot) : Q_h^{k+1} \rightarrow \mathbb{R}$ are obtained by cell-by-cell assembly of the local spatial and temporal discretizations, *i.e.*: For all $\mathbf{v}_h \in \mathbf{V}_h^k$ and all $q_h \in Q_h^{k+1}$,

$$r_{i,h}^{\text{mnt}} \left((\mathbf{u}_h(t), p_h(t)); \mathbf{v}_h \right) := \sum_{T \in \mathcal{T}_h} std_{i,T}^{\text{mnt}} \left((\mathbf{u}_T(t), p_T(t)); \mathbf{v}_T \right),$$

$$r_{i,h}^{\text{cnt}}(\mathbf{u}_h(t); q_h) := \sum_{T \in \mathcal{T}_h} std_{i,T}^{\text{cnt}}(\mathbf{u}_T(t); q_T).$$

The ESDIRK i th-stage problem, that is the time discrete counterpart of problem (6), reads: Given $\mathbf{u}_h|_{t+\delta t_j}, p_h|_{t+\delta t_j}$, with $j = 1, \dots, i-1$, find $\mathbf{u}_h|_{t+\delta t_i}, p_h|_{t+\delta t_i}$ such that

$$r_{i,h}^{\text{mnt}} \left((\mathbf{u}_h(t), p_h(t)); \mathbf{v}_h \right) = 0 \quad \forall \mathbf{v}_h \in \mathbf{V}_h^k, \quad \text{and} \quad r_{i,h}^{\text{cnt}}(\mathbf{u}_h(t); q_h) = 0 \quad \forall q_h \in Q_h^{k+1}. \quad (10)$$

The solution of the above problem can be sought by means of Newton's method. Introducing the shortcut notations $\mathbf{v}_T \leftarrow (\mathbf{v}_T, (\mathbf{0})_{F \in \mathcal{F}_T})$ and $\mathbf{v}_{\partial T} \leftarrow (\mathbf{0}, (\mathbf{v}_F)_{F \in \mathcal{F}_T})$ in the second argument of $std_{i,T}^{\text{mnt}}$, and $q_T \leftarrow (q_T, (0)_{F \in \mathcal{F}_T})$ and $q_{\partial T} \leftarrow$

$(0, (q_F)_{F \in \mathcal{F}_T})$ in the second argument of $std_{i,T}^{\text{cnt}}$, the Newton's algorithm for solving (10) reads: Find $\delta \underline{\mathbf{u}}_h, \delta \underline{\mathbf{p}}_h$ such that

$$\begin{aligned}
& - \sum_{T \in \mathcal{T}_h} \left(\begin{bmatrix} std_{i,T}^{\text{mnt}}((\underline{\mathbf{u}}_T(t), \underline{\mathbf{p}}_T(t)); \mathbf{v}_T) \\ std_{i,T}^{\text{mnt}}((\underline{\mathbf{u}}_T(t), \underline{\mathbf{p}}_T(t)); \mathbf{v}_{\partial T}) \\ std_{i,T}^{\text{cnt}}(\underline{\mathbf{u}}_T(t); q_T) \\ std_{i,T}^{\text{cnt}}(\underline{\mathbf{u}}_T(t); q_{\partial T}) \end{bmatrix} \right) \\
& = \sum_{T \in \mathcal{T}_h} \left(\begin{bmatrix} \frac{\partial std_{i,T}^{\text{mnt}}((\underline{\mathbf{u}}_T(t), \underline{\mathbf{p}}_T(t)); \mathbf{v}_T)}{\partial \underline{\mathbf{u}}_T|_{t+\delta t_i}} & \frac{\partial std_{i,T}^{\text{mnt}}((\underline{\mathbf{u}}_T(t), \underline{\mathbf{p}}_T(t)); \mathbf{v}_T)}{\partial \underline{\mathbf{u}}_{\partial T}|_{t+\delta t_i}} & \frac{\partial std_{i,T}^{\text{mnt}}((\underline{\mathbf{u}}_T(t), \underline{\mathbf{p}}_T(t)); \mathbf{v}_T)}{\partial p_T|_{t+\delta t_i}} & \frac{\partial std_{i,T}^{\text{mnt}}((\underline{\mathbf{u}}_T(t), \underline{\mathbf{p}}_T(t)); \mathbf{v}_T)}{\partial p_{\partial T}|_{t+\delta t_i}} \\ \frac{\partial std_{i,T}^{\text{mnt}}((\underline{\mathbf{u}}_T(t), \underline{\mathbf{p}}_T(t)); \mathbf{v}_{\partial T})}{\partial \underline{\mathbf{u}}_T|_{t+\delta t_i}} & \frac{\partial std_{i,T}^{\text{mnt}}((\underline{\mathbf{u}}_T(t), \underline{\mathbf{p}}_T(t)); \mathbf{v}_{\partial T})}{\partial \underline{\mathbf{u}}_{\partial T}|_{t+\delta t_i}} & \frac{\partial std_{i,T}^{\text{mnt}}((\underline{\mathbf{u}}_T(t), \underline{\mathbf{p}}_T(t)); \mathbf{v}_{\partial T})}{\partial p_T|_{t+\delta t_i}} & \frac{\partial std_{i,T}^{\text{mnt}}((\underline{\mathbf{u}}_T(t), \underline{\mathbf{p}}_T(t)); \mathbf{v}_{\partial T})}{\partial p_{\partial T}|_{t+\delta t_i}} \\ \frac{\partial std_{i,T}^{\text{cnt}}(\underline{\mathbf{u}}_T(t); q_T)}{\partial \underline{\mathbf{u}}_T|_{t+\delta t_i}} & \frac{\partial std_{i,T}^{\text{cnt}}(\underline{\mathbf{u}}_T(t); q_T)}{\partial \underline{\mathbf{u}}_{\partial T}|_{t+\delta t_i}} & \frac{\partial std_{i,T}^{\text{cnt}}(\underline{\mathbf{u}}_T(t); q_T)}{\partial p_T|_{t+\delta t_i}} & \frac{\partial std_{i,T}^{\text{cnt}}(\underline{\mathbf{u}}_T(t); q_T)}{\partial p_{\partial T}|_{t+\delta t_i}} \\ \frac{\partial std_{i,T}^{\text{cnt}}(\underline{\mathbf{u}}_T(t); q_{\partial T})}{\partial \underline{\mathbf{u}}_T|_{t+\delta t_i}} & \frac{\partial std_{i,T}^{\text{cnt}}(\underline{\mathbf{u}}_T(t); q_{\partial T})}{\partial \underline{\mathbf{u}}_{\partial T}|_{t+\delta t_i}} & \frac{\partial std_{i,T}^{\text{cnt}}(\underline{\mathbf{u}}_T(t); q_{\partial T})}{\partial p_T|_{t+\delta t_i}} & \frac{\partial std_{i,T}^{\text{cnt}}(\underline{\mathbf{u}}_T(t); q_{\partial T})}{\partial p_{\partial T}|_{t+\delta t_i}} \end{bmatrix} \begin{bmatrix} \delta \underline{\mathbf{u}}_T \\ \delta \underline{\mathbf{u}}_{\partial T} \\ \delta p_T \\ \delta p_{\partial T} \end{bmatrix} \right) \quad (11)
\end{aligned}$$

replace $\underline{\mathbf{u}}_h|_{t+\delta t_i} \leftarrow \underline{\mathbf{u}}_h|_{t+\delta t_i} + \delta \underline{\mathbf{u}}_h, \underline{\mathbf{p}}_h|_{t+\delta t_i} \leftarrow \underline{\mathbf{p}}_h|_{t+\delta t_i} + \delta \underline{\mathbf{p}}_h$ until $\delta \underline{\mathbf{u}}_h, \delta \underline{\mathbf{p}}_h$ is small enough. The local Jacobian matrix on the left hand side can be computed cell-by-cell and assembled into the global Jacobian matrix. Nevertheless, in order to improve efficiency of the solution strategy and reduce the memory footprint of ESDIRK-HHO formulations, static condensation strategies can be fruitfully exploited, as described in the next section.

3.6 Algebraic expression for Newton's method and static condensation

The unknowns for a mesh cell $T \in \mathcal{T}_h$ correspond to the coefficients of the expansions of the velocity and pressure in the selected local bases. Assuming that the unknowns are ordered so that cell velocities come first and boundary velocities next, these coefficients are collected in the vectors

$$\underline{\mathbf{U}}_T = \begin{bmatrix} \mathbf{U}_T \\ \mathbf{U}_{\partial T} \end{bmatrix} \text{ and } \underline{\mathbf{P}}_T = \begin{bmatrix} \mathbf{P}_T \\ \mathbf{P}_{\partial T} \end{bmatrix},$$

where the block partition is the one naturally induced by the selected ordering of unknowns.

Let's introduce the vector representations $\underline{\mathbf{D}}_T^{\text{mnt}} = \begin{bmatrix} \mathbf{D}_T^{\text{mnt}} \\ \mathbf{D}_{\partial T}^{\text{mnt}} \end{bmatrix}$ and $\underline{\mathbf{D}}_T^{\text{cnt}} = \begin{bmatrix} \mathbf{D}_T^{\text{cnt}} \\ \mathbf{D}_{\partial T}^{\text{cnt}} \end{bmatrix}$ of the local spatial and temporal discretizations $std_{i,T}^{\text{mnt}}((\underline{\mathbf{u}}_T(t), \underline{\mathbf{p}}_T(t)); \mathbf{v}_T)$, $std_{i,T}^{\text{cnt}}(\underline{\mathbf{u}}_T(t); q_T)$ defined in (8). The block partition is the one induced by mimicking the selected ordering of unknowns for the expansion bases.

Let's also introduce the matrix representation of the relevant blocks of the local Jacobian matrix in (11)

$$\begin{aligned}
\begin{bmatrix} \mathbf{A}_{TT} & \mathbf{A}_{T\partial T} \\ \mathbf{A}_{\partial TT} & \mathbf{A}_{\partial T\partial T} \end{bmatrix} & \sim \begin{bmatrix} \frac{\partial std_{i,T}^{\text{mnt}}((\underline{\mathbf{u}}_T(t), \underline{\mathbf{p}}_T(t)); \mathbf{v}_T)}{\partial \underline{\mathbf{u}}_T|_{t+\delta t_i}} & \frac{\partial std_{i,T}^{\text{mnt}}((\underline{\mathbf{u}}_T(t), \underline{\mathbf{p}}_T(t)); \mathbf{v}_T)}{\partial \underline{\mathbf{u}}_{\partial T}|_{t+\delta t_i}} \\ \frac{\partial std_{i,T}^{\text{mnt}}((\underline{\mathbf{u}}_T(t), \underline{\mathbf{p}}_T(t)); \mathbf{v}_{\partial T})}{\partial \underline{\mathbf{u}}_T|_{t+\delta t_i}} & \frac{\partial std_{i,T}^{\text{mnt}}((\underline{\mathbf{u}}_T(t), \underline{\mathbf{p}}_T(t)); \mathbf{v}_{\partial T})}{\partial \underline{\mathbf{u}}_{\partial T}|_{t+\delta t_i}} \end{bmatrix}, \\
\begin{bmatrix} \mathbf{B}_{TT} & \mathbf{0} \\ \mathbf{B}_{\partial TT} & \mathbf{B}_{\partial T\partial T} \end{bmatrix} & \sim \begin{bmatrix} \frac{\partial std_{i,T}^{\text{cnt}}(\underline{\mathbf{u}}_T(t); q_T)}{\partial \underline{\mathbf{u}}_T|_{t+\delta t_i}} & \frac{\partial std_{i,T}^{\text{cnt}}(\underline{\mathbf{u}}_T(t); q_T)}{\partial \underline{\mathbf{u}}_{\partial T}|_{t+\delta t_i}} \\ \frac{\partial std_{i,T}^{\text{cnt}}(\underline{\mathbf{u}}_T(t); q_{\partial T})}{\partial \underline{\mathbf{u}}_T|_{t+\delta t_i}} & \frac{\partial std_{i,T}^{\text{cnt}}(\underline{\mathbf{u}}_T(t); q_{\partial T})}{\partial \underline{\mathbf{u}}_{\partial T}|_{t+\delta t_i}} \end{bmatrix}.
\end{aligned}$$

The matrices on the left are obtained from the terms on the right by plugging local expansions and bases in the spatial-temporal discretizations. Notice that also the derivatives with respect to velocity and pressure should be replaced with derivatives computed with respect to the coefficients of the expansions in the corresponding local bases.

According to the notation above, the algebraic counterpart of problem (11) reads

$$- \sum_{T \in \mathcal{T}_h} \left(\begin{bmatrix} \mathbf{D}_T^{\text{mnt}} \\ \mathbf{D}_{\partial T}^{\text{mnt}} \\ \mathbf{D}_T^{\text{cnt}} \\ \mathbf{D}_{\partial T}^{\text{cnt}} \end{bmatrix} \right) = \sum_{T \in \mathcal{T}_h} \left(\begin{bmatrix} \mathbf{A}_{TT} & \mathbf{A}_{T\partial T} & \mathbf{B}_{TT}^\top & \mathbf{B}_{\partial TT}^\top \\ \mathbf{A}_{\partial TT} & \mathbf{A}_{\partial T\partial T} & \mathbf{0} & \mathbf{B}_{\partial T\partial T}^\top \\ \mathbf{B}_{TT} & \mathbf{0} & \mathbf{0} & \mathbf{0} \\ \mathbf{B}_{\partial TT} & \mathbf{B}_{\partial T\partial T} & \mathbf{0} & \mathbf{0} \end{bmatrix} \begin{bmatrix} \delta \mathbf{U}_T \\ \delta \mathbf{U}_{\partial T} \\ \delta \mathbf{P}_T \\ \delta \mathbf{P}_{\partial T} \end{bmatrix} \right)$$

and, rearranging the unknowns and equations, the local problem can be rewritten as follows

$$- \sum_{T \in \mathcal{T}_h} \left(\begin{bmatrix} \mathbf{D}_T^{\text{mnt}} \\ \mathbf{D}_{\partial T}^{\text{mnt}} \\ \mathbf{D}_T^{\text{cnt}} \\ \mathbf{D}_{\partial T}^{\text{cnt}} \end{bmatrix} \right) = \sum_{T \in \mathcal{T}_h} \left(\begin{bmatrix} \mathbf{A}_{TT} & \mathbf{B}_{TT}^\top & \mathbf{A}_{T\partial T} & \mathbf{B}_{\partial TT}^\top \\ \mathbf{B}_{TT} & \mathbf{0} & \mathbf{0} & \mathbf{0} \\ \mathbf{A}_{\partial TT} & \mathbf{0} & \mathbf{A}_{\partial T\partial T} & \mathbf{B}_{\partial T\partial T}^\top \\ \mathbf{B}_{\partial TT} & \mathbf{0} & \mathbf{B}_{\partial T\partial T} & \mathbf{0} \end{bmatrix} \begin{bmatrix} \delta \mathbf{U}_T \\ \delta \mathbf{P}_T \\ \delta \mathbf{U}_{\partial T} \\ \delta \mathbf{P}_{\partial T} \end{bmatrix} \right). \quad (12)$$

The only unknowns that are globally coupled are those collected in the subvector $\begin{bmatrix} \delta \mathbf{U}_{\partial T} \\ \delta \mathbf{P}_{\partial T} \end{bmatrix}$, while the remaining unknowns collected in $\begin{bmatrix} \delta \mathbf{U}_T \\ \delta \mathbf{P}_T \end{bmatrix}$ can be eliminated by expressing them in terms of the former. After performing this local elimination, the algebraic counterpart of the Newton method reads

$$-\sum_{T \in \mathcal{T}_h} \left(\begin{bmatrix} \mathbf{D}_{\partial T}^{\text{mnt}} \\ \mathbf{D}_{\partial T}^{\text{cnt}} \end{bmatrix} - \begin{bmatrix} \mathbf{A}_{\partial TT} & \mathbf{0} \\ \mathbf{B}_{\partial TT} & \mathbf{0} \end{bmatrix} \begin{bmatrix} \mathbf{A}_{TT} & \mathbf{B}_{TT}^\top \\ \mathbf{B}_{TT} & \mathbf{0} \end{bmatrix}^{-1} \begin{bmatrix} \mathbf{D}_T^{\text{mnt}} \\ \mathbf{D}_T^{\text{cnt}} \end{bmatrix} \right) = \sum_{T \in \mathcal{T}_h} \left(\mathbf{S}_T \begin{bmatrix} \delta \mathbf{U}_{\partial T} \\ \delta \mathbf{P}_{\partial T} \end{bmatrix} \right),$$

where \mathbf{S}_T denotes the Schur complement of the top left block of the left-hand side matrix in (12), that is,

$$\mathbf{S}_T = \mathbf{S}_{\partial T \partial T} := \begin{bmatrix} \mathbf{A}_{\partial T \partial T} & \mathbf{B}_{\partial T \partial T}^\top \\ \mathbf{B}_{\partial T \partial T} & \mathbf{0} \end{bmatrix} - \begin{bmatrix} \mathbf{A}_{\partial TT} & \mathbf{0} \\ \mathbf{B}_{\partial TT} & \mathbf{0} \end{bmatrix} \begin{bmatrix} \mathbf{A}_{TT} & \mathbf{B}_{TT}^\top \\ \mathbf{B}_{TT} & \mathbf{0} \end{bmatrix}^{-1} \begin{bmatrix} \mathbf{A}_{T \partial T} & \mathbf{B}_{\partial TT}^\top \\ \mathbf{0} & \mathbf{0} \end{bmatrix}.$$

When increasing the polynomial degree k , the dimension of polynomial spaces over mesh cells grows much faster than the dimension of polynomial spaces over mesh faces. Accordingly, the possibility to statically condense the cells unknowns is the key for achieving efficiency when high-order accurate formulations are employed. In order to further improve the performance of the iterative linear solver required for the solution of each Newton step we rely on the p -multilevel preconditioner strategy proposed in [11].

3.7 Time step adaptation

Local time step adaptation enables step-by-step control of the time integration error. The key element of the adaptation procedure is an estimator of the temporal discretization error, thus, based on the temporal error metric and a user defined threshold tolerance, the time step can be increased or reduced and the solution can be accepted or recomputed in order to meet the prescribed precision.

Let $\mathbf{u}_h|_t \in L^2(\Omega)^d$ and $p_h|_t \in L^2(\Omega)$ be the discrete velocity and pressure solution at time t , obtained by gluing together the cell components. The time integration error is computed as:

$$r = \|\mathbf{u}_h|_{t+\delta t} - \hat{\mathbf{u}}_h|_{t+\delta t}\|_{L^2(\Omega)} + \|p_h|_{t+\delta t} - \hat{p}_h|_{t+\delta t}\|_{L^2(\Omega)},$$

where both $\mathbf{u}_h|_{t+\delta t}$, $p_h|_{t+\delta t}$, and $\hat{\mathbf{u}}_h|_{t+\delta t}$, $\hat{p}_h|_{t+\delta t}$ are computed by means of a s -stages ESDIRK time integration strategy, but the less accurate solution $\hat{\mathbf{u}}_h|_{t+\delta t}$, $\hat{p}_h|_{t+\delta t}$ is obtained by replacing the ESDIRK coefficients b_i in (7) with a different set of coefficients \hat{b}_i , for $i = 1, \dots, s$. In the ESDIRK nomenclature, $\hat{\mathbf{u}}_h|_{t+\delta t}$, $\hat{p}_h|_{t+\delta t}$ is referred as the *embedded* solution.

Following [35, 36], at the end of each ESDIRK stage, we require that

$$r < \mu \text{tol}_a. \quad (13)$$

where tol_a is the user-defined threshold tolerance and μ is a safety factor, which we take here equal to $\sqrt{10}$. Accordingly, if condition (13) is met, the solution is accepted, otherwise, the solution is rejected and a new solution $\mathbf{u}_h|_{t+\delta t}$, $p_h|_{t+\delta t}$ is computed restarting the time marching strategy from the previous step solution $\mathbf{u}_h|_t$, $p_h|_t$ and reducing the time step.

Several strategies for tailoring the time step are available in the literature, see [23, 27, 35, 31, 22] for some examples. In this work, the time step update δt_u is computed as follows

$$\delta t_u = \left(\frac{\text{tol}_a}{r} \right)^{\frac{1}{q}} \delta t, \quad (14)$$

where q is the order of accuracy of the error estimator r , which matches the order of accuracy of the embedded solution. Notice that a time step reduction is guaranteed if the solution is rejected, i.e., $r > \mu \text{tol}_a$. Moreover, in order to prevent excessive time step fluctuations, the following limiter function is introduced

$$\delta t_l = \delta t \left[1 + \kappa \operatorname{atan} \left(\frac{\delta t_u - \delta t}{\kappa \delta t} \right) \right], \quad (15)$$

where the free parameter κ controls the limiting strategy. In this work, κ is chosen such that the maximum acceptable time step relaxation ensures a one order of magnitude increase in the time integration error, i.e.,

$$\kappa = \frac{2}{\pi} \left(10^{\frac{1}{q}} - 1 \right).$$

Upon completion of a time step, regardless of whether the solution is accepted or rejected, the new time step is computed applying (14) and (15), and, thus, setting $\delta t = \delta t_l$.

4 Numerical validation

Let us briefly describe the numerical setup common to the test cases presented in what follows. Numerical integration over mesh cells and mesh faces is performed over standardized reference cells based on Gaussian quadrature rules. Reference-to-physical-frame mappings from reference entities to mesh entities are defined by means of Lagrange polynomials. Discrete polynomial spaces over mesh cells and mesh faces are spanned by orthonormal modal bases. Specifically, we rely on physical frame polynomial spaces over mesh cells and reference frame polynomial spaces over mesh faces, as proposed in [6]. Orthogonalization in the physical frame is performed cell-by-cell starting from a monomial basis defined in a local reference frame aligned with the principal axes of inertia of each mesh cell, as described in [3].

Simultaneous multi-process execution of the code is achieved partitioning the computational grid, such that the number of mesh partitions matches the number of processes, and relying on the Message Passing Interface (MPI) to synchronize and exchange data among the processes. Scalability of the iterative solvers applied for the resolution of algebraic problems is pursued relying on the PETSc library [2]. In particular, we apply one sweep of p -multigrid V-cycle as a preconditioner for the FGMRES (flexible GMRES) iteration. As a smoothing strategy within the V-cycle we rely on a few iterations of GMRES and we employ additive Schwarz method (ASM) preconditioners to further improve performance in parallel. All applications of prolongation and restriction operators involved in the V-cycle iteration are performed matrix-free, that is, without assembling the global sparse matrices associated to the operators, see [7] for details.

4.1 Travelling waves

In order to numerically assess the spatial and temporal convergence rates of the ESDIRK-HHO formulation, we consider the following 2D dimensionless damped travelling waves solution of the Navier–Stokes equations:

$$\begin{aligned} u(x, y, t) &= 1 + 2 \cos(2\pi(x - t)) \sin(2\pi(y - t)) e^{-8\pi^2 \nu t}, \\ v(x, y, t) &= 1 - 2 \sin(2\pi(x - t)) \cos(2\pi(y - t)) e^{-8\pi^2 \nu t}, \\ p(x, y, t) &= -[\cos(4\pi(x - t)) + \cos(4\pi(y - t))] e^{-16\pi^2 \nu t}, \end{aligned}$$

where u and v are the velocity components in the x and y directions, respectively, p is the pressure and t is the time. The computational domain is the unit square $\Omega = [0.25, 1.25] \times [0.5, 1.5]$ and time integration is carried out in the interval $[0, 1]$. Accordingly the errors in L^2 norm for the velocity, the velocity gradients and the pressure are computed based on the exact solution at the final time $t_F = 1$. Periodic boundary conditions are enforced on $\partial\Omega$ and the velocity field is initialized interpolating the exact solution. We rely on triangular cells meshes obtained subdividing in two right triangles the square cells of N^2 Cartesian grids, with N cells per Cartesian direction. Accordingly, the mesh cardinality is $\text{card}(\mathcal{T}_h) = 2N^2$ when $h = \frac{\sqrt{2}}{N}$.

The temporal accuracy is tested with $\nu = \text{Re}^{-1} = 10^{-2}$ based on a $k = 9$ HHO formulation on a triangular cells mesh with $N = 8$ and $\text{card}(\mathcal{T}_h) = 128$. The results are reported in Table 1 considering $\delta t = \frac{0.1}{2^i}$, $i = 0, \dots, 4$, and ESDIRK schemes with third, fourth and fifth order of accuracy. The numerical convergence rates clearly replicate the expected rates of error reduction. It is interesting to notice that the pressure error in the L^2 -norm stagnates around a precision of 10^{-9} . We remark that, due to the use of periodic boundary conditions, the pressure mean value needs to be pinned by means of the Lagrange multipliers method. Also the pressure gradient error in L^2 norm is reported.

The spatial accuracy is tested varying the viscosity, up to the inviscid limit. In particular, we set $\nu = 10^{-1, -3, -6, -13}$ in order to cover both the viscous dominated and the convection-dominated flow regimes. The results are reported in Tables 2–5 for $k = 1, 2, 3, 4$ HHO formulations, respectively, considering triangular meshes with $N = 4 \times 2^i$, $i = 0, \dots, 4$. In the case $k = 1$, we consider an additional finer mesh with $N = 4 \times 2^5$. Time integration is performed relying on a fifth order accurate ESDIRK scheme with time step $\delta t = 1/400$. A $k + 1$ rate of error reduction is observed for the pressure error in the L^2 norm, both in the diffusion-dominated and convection-dominated regimes. On the other hand, the velocity and velocity gradient errors in L^2 norm show rates of convergence of $k + 2$ and $k + 1$, respectively, in the diffusion-dominated regime, whereas the rate of error reduction is reduced by one in the convection-dominated regime.

4.2 Double shear layer

The double shear layer problem, introduced in [5], is employed to assess the ESDIRK-HHO formulation in the context of unsteady inviscid flows (i.e., $\nu = 0$). The computational domain is double periodic unit square, $\Omega = (0, 1) \times (0, 1)$ and time integration is carried out over the time interval $[t_0 = 0, t_F = 2]$. The initial conditions for the horizontal and vertical velocity components read

$$u = \begin{cases} \tanh\left(\frac{y - 0.25}{\xi}\right) & \text{if } y \leq 0.5, \\ \tanh\left(\frac{0.75 - y}{\xi}\right) & \text{if } y > 0.5 \end{cases} \quad \text{and} \quad v = \delta \sin(2\pi x),$$

respectively. Free parameters are set as $\xi = 1/30$ and $\delta = 1/20$.

δt	$\ \nabla \mathbf{u}_h\ _{L^2(\Omega)}$	rate	$\ \mathbf{u}_h\ _{L^2(\Omega)}$	rate	$\ \nabla p_h\ _{L^2(\Omega)}$	rate	$\ p_h\ _{L^2(\Omega)}$	rate	$\ \nabla \cdot \mathbf{u}_h\ _{L^2(\Omega)}$
0.1	1.5621	–	0.1758	–	1.0031	–	0.07982	–	2.26e-12
0.05	0.2832	2.46	0.03187	2.46	0.1818	2.46	0.01447	2.46	1.60e-12
0.025	0.03938	2.85	0.004432	2.85	0.02528	2.85	0.002012	2.85	6.08e-13
0.0125	0.005063	2.96	0.0005698	2.96	0.003251	2.96	0.0002587	2.96	2.60e-14
0.00625	0.0006381	2.99	7.1820e-05	2.99	0.0004097	2.99	3.2609e-05	2.99	3.30e-15
0.1	0.10181	–	0.01145	–	0.06537	–	0.005202	–	4.83e-12
0.05	0.006672	3.93	0.0007509	3.93	0.004284	3.93	0.0003409	3.93	1.20e-12
0.025	0.0004210	3.99	4.7386e-05	3.99	0.0002703	3.99	2.1515e-05	3.99	6.54e-14
0.0125	2.6370e-05	4.00	2.9677e-06	4.00	1.6932e-05	4.00	1.3474e-06	4.00	1.57e-13
0.00625	1.6488e-06	4.00	1.8555e-07	4.00	1.0586e-06	4.00	8.4531e-08	3.99	3.03e-14
0.1	0.01553	–	0.001748	–	0.009977	–	0.0007939	–	6.46e-12
0.05	0.0005485	4.82	6.1735e-05	4.82	0.0003522	4.82	2.8030e-05	4.82	1.51e-12
0.025	1.7765e-05	4.95	1.9992e-06	4.95	1.1407e-05	4.95	9.0776e-07	4.95	4.32e-13
0.0125	5.6137e-07	4.98	6.3176e-08	4.98	3.6062e-07	4.98	2.8768e-08	4.98	4.33e-13
0.00625	1.7691e-08	4.99	1.9818e-09	4.99	1.1676e-08	4.95	9.551e-09	1.59	2.36e-13

Table 1: Numerical validation of third, fourth and fifth order accurate ESDIRK time integration strategies (first, second and third bunch of rows, respectively) based on the travelling waves analytical solution, $\nu = 0.01$. $L^2(\Omega)$ error norms with respect to the exact solution and the corresponding rates of convergence while halving the time step δt are reported. The spatial discretization is chosen such that the spatial approximation error is negligible, see text for details.

ν	card(\mathcal{T}_h)	$\ \nabla \mathbf{u}_h\ _{L^2(\Omega)}$	rate	$\ \mathbf{u}_h\ _{L^2(\Omega)}$	rate	$\ \nabla p_h\ _{L^2(\Omega)}$	rate	$\ p_h\ _{L^2(\Omega)}$	rate	$\ \nabla \cdot \mathbf{u}_h\ _{L^2(\Omega)}$
0.1	32	0.001203	–	6.7983e-05	–	0.0003894	–	1.9758e-05	–	9.41e-14
0.001	32	5.4322	–	0.5410	–	6.2631	–	0.4732	–	5.78e-13
1e-06	32	6.0543	–	0.6051	–	7.4717	–	0.5723	–	7.55e-13
1e-13	32	6.0550	–	0.6051	–	7.4730	–	0.5724	–	5.69e-13
0.1	128	0.0002875	2.07	7.3658e-06	3.21	0.0001814	1.10	4.3497e-06	2.18	2.14e-12
0.001	128	1.5872	1.78	0.06885	2.97	4.0687	0.62	0.09117	2.38	5.68e-13
1e-06	128	1.8024	1.75	0.07377	3.04	4.7664	0.65	0.107	2.42	1.81e-13
1e-13	128	1.8026	1.75	0.07377	3.04	4.7672	0.65	0.1070	2.42	1.77e-13
0.1	512	7.3274e-05	1.97	1.0219e-06	2.85	7.6092e-05	1.25	8.9064e-07	2.29	8.11e-13
0.001	512	0.7405	1.10	0.01300	2.40	2.0728	0.97	0.01926	2.24	3.15e-13
1e-06	512	0.8820	1.03	0.01567	2.23	2.4282	0.97	0.02329	2.20	2.92e-13
1e-13	512	0.8822	1.03	0.01567	2.23	2.4286	0.97	0.02329	2.20	2.79e-13
0.1	2048	1.8747e-05	1.97	1.4007e-07	2.87	3.39076e-05	1.17	1.9793e-07	2.17	9.39e-13
0.001	2048	0.3413	1.12	0.002149	2.60	1.0430	0.99	0.004269	2.18	5.73e-13
1e-06	2048	0.4173	1.08	0.002694	2.54	1.2217	0.99	0.005065	2.20	4.06e-13
1e-13	2048	0.4174	1.08	0.002695	2.54	1.2219	0.99	0.005066	2.20	3.32e-13
0.1	8192	4.7637e-06	1.98	1.8454e-08	2.92	1.5934e-05	1.09	4.6720e-08	2.08	8.43e-13
0.001	8192	0.1580	1.11	0.0004015	2.42	0.5221	1.00	0.001018	2.07	6.08e-13
1e-06	8192	0.2022	1.05	0.0005448	2.31	0.6120	1.00	0.001203	2.07	3.69e-13
1e-13	8192	0.2023	1.05	0.0005451	2.31	0.6121	1.00	0.001203	2.07	5.72e-13
0.1	32768	1.2023e-06	1.99	2.3710e-09	2.96	7.7197e-06	1.05	1.1368e-08	2.04	1.75e-12
0.001	32768	0.06972	1.18	8.0120e-05	2.33	0.2610	1.00	0.0002509	2.02	3.42e-13
1e-06	32768	0.09930	1.03	0.0001257	2.11	0.3061	1.00	0.0002962	2.02	8.98e-13
1e-13	32768	0.09937	1.03	0.0001258	2.11	0.3062	1.00	0.0002962	2.02	7.53e-13

Table 2: Numerical validation of spatial convergence of $k = 1$ HHO formulations based on the 2D travelling waves analytical solution of the INS equations. $L^2(\Omega)$ error norms with respect to the exact solution and the corresponding rates of convergence while halving the mesh step size are reported. The temporal discretization is chosen such that the temporal approximation error is negligible, see text for details.

ν	$\text{card}(\mathcal{T}_h)$	$\ \nabla \mathbf{u}_h\ _{L^2(\Omega)}$	rate	$\ \mathbf{u}_h\ _{L^2(\Omega)}$	rate	$\ \nabla p_h\ _{L^2(\Omega)}$	rate	$\ p_h\ _{L^2(\Omega)}$	rate	$\ \nabla \cdot \mathbf{u}_h\ _{L^2(\Omega)}$
0.1	32	0.0002957	–	5.0485e-06	–	8.5890e-05	–	2.7305e-06	–	5.72e-13
0.001	32	1.2582	–	0.09389	–	3.8927	–	0.09868	–	4.13e-13
1e-06	32	1.4981	–	0.1205	–	4.5655	–	0.1205	–	1.72e-13
1e-13	32	1.4985	–	0.1206	–	4.5662	–	0.1205	–	1.70e-13
0.1	128	4.2158e-05	2.81	3.2873e-07	3.94	2.5555e-05	1.75	5.2560e-07	2.38	9.29e-14
0.001	128	0.2174	2.53	0.004007	4.55	0.82091	2.25	0.008018	3.62	7.65e-13
1e-06	128	0.2652	2.50	0.005258	4.52	0.9616	2.25	0.009493	3.67	5.76e-13
1e-13	128	0.2652	2.50	0.005260	4.52	0.9618	2.25	0.009495	3.67	5.77e-13
0.1	512	5.6570e-06	2.90	2.1588e-08	3.93	7.0716e-06	1.85	8.1220e-08	2.69	3.98e-12
0.001	512	0.04275	2.35	0.0003418	3.55	0.2099	1.97	0.0009949	3.01	2.31e-13
1e-06	512	0.05460	2.28	0.0005395	3.28	0.2457	1.97	0.001180	3.01	8.13e-13
1e-13	512	0.05461	2.28	0.0005397	3.28	0.2458	1.97	0.001180	3.01	8.22e-13
0.1	2048	7.3152e-07	2.95	1.3850e-09	3.96	1.8653e-06	1.92	1.0957e-08	2.89	2.11e-12
0.001	2048	0.009498	2.17	3.0208e-05	3.50	0.05275	1.99	0.0001240	3.00	3.15e-13
1e-06	2048	0.01363	2.00	6.2722e-05	3.10	0.06176	1.99	0.0001466	3.01	6.04e-13
1e-13	2048	0.01364	2.00	6.2821e-05	3.10	0.06177	1.99	0.0001466	3.01	6.28e-13
0.1	8192	9.2932e-08	2.98	8.7751e-11	3.98	4.8126e-07	1.95	1.4122e-09	2.96	2.59e-13
0.001	8192	0.002072	2.20	3.1228e-06	3.27	0.01320	2.00	1.551e-05	3.00	1.03e-12
1e-06	8192	0.003424	1.99	7.5234e-06	3.06	0.01545	2.00	1.8263e-05	3.01	4.10e-13
1e-13	8192	0.003432	1.99	7.5691e-06	3.05	0.01546	2.00	1.8267e-05	3.01	4.57e-13

Table 3: Numerical validation of spatial convergence of $k = 2$ HHO formulations based on the 2D travelling waves analytical solution of the INS equations. $L^2(\Omega)$ error norms with respect to the exact solution and the corresponding rates of convergence while halving the mesh step size are reported. The temporal discretization is chosen such that the temporal approximation error is negligible, see text for details.

ν	$\text{card}(\mathcal{T}_h)$	$\ \nabla \mathbf{u}_h\ _{L^2(\Omega)}$	rate	$\ \mathbf{u}_h\ _{L^2(\Omega)}$	rate	$\ \nabla p_h\ _{L^2(\Omega)}$	rate	$\ p_h\ _{L^2(\Omega)}$	rate	$\ \nabla \cdot \mathbf{u}_h\ _{L^2(\Omega)}$
0.1	32	6.6228e-05	–	7.2412e-07	–	3.8257e-05	–	8.4398e-07	–	2.81e-13
0.001	32	0.2132	–	0.01085	–	0.3599	–	0.006474	–	2.20e-13
1e-06	32	0.2587	–	0.01696	–	0.4296	–	0.008612	–	3.37e-13
1e-13	32	0.2587	–	0.01697	–	0.4297	–	0.008615	–	3.37e-13
0.1	128	4.6237e-06	3.84	2.4960e-08	4.86	5.1633e-06	2.89	8.2597e-08	3.35	1.02e-12
0.001	128	0.02822	2.92	0.0003635	4.90	0.1139	1.66	0.0007859	3.04	9.75e-13
1e-06	128	0.03719	2.80	0.0006228	4.77	0.1334	1.69	0.0009419	3.19	5.24e-13
1e-13	128	0.03720	2.80	0.0006236	4.77	0.1334	1.69	0.0009421	3.19	5.14e-13
0.1	512	3.0449e-07	3.92	8.2613e-10	4.92	6.7674e-07	2.93	1.4546e-08	2.51	1.36e-12
0.001	512	0.003378	3.06	1.7164e-05	4.40	0.01455	2.97	4.8836e-05	4.01	5.15e-13
1e-06	512	0.004658	3.00	3.2885e-05	4.24	0.01707	2.97	6.0838e-05	3.95	9.80e-13
1e-13	512	0.004660	3.00	3.2930e-05	4.24	0.01707	2.97	6.0863e-05	3.95	1.01e-12
0.1	2048	1.9567e-08	3.96	2.6658e-11	4.95	8.6238e-08	2.97	3.4509e-10	5.40	2.75e-12
0.001	2048	0.0003887	3.12	8.9600e-07	4.26	0.001827	2.99	3.0508e-06	4.00	6.19e-13
1e-06	2048	0.0005746	3.02	1.8437e-06	4.16	0.002146	2.99	3.6821e-06	4.05	8.36e-13
1e-13	2048	0.0005753	3.02	1.8492e-06	4.15	0.002146	2.99	3.6839e-06	4.05	9.14e-13
0.1	8192	1.2409e-09	3.98	8.4851e-13	4.97	1.0867e-08	2.99	4.6066e-09	-3.74	4.85e-13
0.001	8192	4.2409e-05	3.20	4.7596e-08	4.23	0.0002285	3.00	1.9067e-07	4.00	9.33e-13
1e-06	8192	7.0980e-05	3.02	1.0431e-07	4.14	0.0002687	3.00	2.2579e-07	4.03	1.03e-13
1e-13	8192	7.1130e-05	3.02	1.0495e-07	4.14	0.0002687	3.00	2.2588e-07	4.03	1.08e-13

Table 4: Numerical validation of spatial convergence of $k = 3$ HHO formulations based on the 2D travelling waves analytical solution of the INS equations. $L^2(\Omega)$ error norms with respect to the exact solution and the corresponding rates of convergence while halving the mesh step size are reported. The temporal discretization is chosen such that the temporal approximation error is negligible, see text for details.

ν	$\text{card}(\mathcal{T}_h)$	$\ \nabla \mathbf{u}_h\ _{L^2(\Omega)}$	rate	$\ \mathbf{u}_h\ _{L^2(\Omega)}$	rate	$\ \nabla p_h\ _{L^2(\Omega)}$	rate	$\ p_h\ _{L^2(\Omega)}$	rate	$\ \nabla \cdot \mathbf{u}_h\ _{L^2(\Omega)}$
0.1	32	1.1145e-05	–	9.1253e-08	–	6.5954e-06	–	1.8277e-07	–	4.69e-13
0.001	32	0.04520	–	0.0009695	–	0.2430	–	0.002501	–	2.80e-13
1e-06	32	0.05847	–	0.001317	–	0.2845	–	0.002945	–	1.57e-13
1e-13	32	0.05848	–	0.001317	–	0.2846	–	0.002946	–	1.44e-13
0.1	128	4.1009e-07	4.76	1.6648e-09	5.78	4.6360e-07	3.83	1.3766e-08	3.73	1.53e-13
0.001	128	0.002186	4.37	1.8281e-05	5.73	0.01180	4.36	5.9362e-05	5.40	2.92e-13
1e-06	128	0.003002	4.28	3.0154e-05	5.45	0.01382	4.36	6.9844e-05	5.40	1.73e-13
1e-13	128	0.003003	4.28	3.0186e-05	5.45	0.01382	4.36	6.9856e-05	5.40	1.84e-13
0.1	512	1.3971e-08	4.88	2.8228e-11	5.88	2.992e-08	3.95	9.3601e-09	0.56	3.33e-13
0.001	512	0.0001164	4.23	4.3736e-07	5.39	0.0007503	3.98	1.8784e-06	4.98	1.43e-13
1e-06	512	0.0001833	4.03	9.8456e-07	4.94	0.0008787	3.98	2.2001e-06	4.99	1.62e-12
1e-13	512	0.0001835	4.03	9.8936e-07	4.93	0.0008789	3.98	2.2005e-06	4.99	1.64e-12
0.1	2048	4.5513e-10	4.94	4.6166e-13	5.93	1.9066e-09	3.97	3.9348e-09	1.25	2.13e-13
0.001	2048	6.5075e-06	4.16	1.1439e-08	5.26	4.7081e-05	3.99	5.8901e-08	5.00	4.56e-13
1e-06	2048	1.2209e-05	3.91	3.1140e-08	4.98	5.5152e-05	3.99	7.0340e-08	4.97	3.66e-13
1e-13	2048	1.2238e-05	3.91	3.1279e-08	4.98	5.5161e-05	3.99	7.0314e-08	4.97	1.06e-13
0.1	8192	1.5414e-11	4.88	4.5488e-14	3.34	2.1161e-10	3.17	8.4956e-09	-1.11	2.13e-13
0.001	8192	3.4267e-07	4.25	2.9502e-10	5.28	2.9447e-06	4.00	1.8657e-09	4.98	4.91e-13
1e-06	8192	7.8597e-07	3.96	1.0102e-09	4.95	3.4511e-06	4.00	2.2215e-09	4.98	7.27e-13
1e-13	8192	7.9142e-07	3.95	1.0208e-09	4.94	3.4517e-06	4.00	2.2426e-09	4.97	6.49e-13

Table 5: Numerical validation of spatial convergence rates of $k = 4$ HHO formulations, 2D travelling waves analytical solution of the INS equations. $L^2(\Omega)$ error norms with respect to the exact solution and the corresponding rates of convergence while halving the mesh step size are reported. The temporal discretization is chosen such that the temporal approximation error is negligible, see text for details.

i	$\text{card}(\mathcal{T}_h)$	tol_a	$\mathcal{I}_t^\%$
0	32	1e-06	0.02%
1	128	1e-06	0.06%
2	512	1e-07	0.03%
3	2048	1e-08	0.02%
4	8192	1e-08	0.79%
5	32768	1e-09	0.27%
6	131072	1e-10	0.36%

Table 6: Double shear layer, $k = 4$ ESDIRK-HHO with local time step adaptation. Adaptation trigger tolerance (tol_a) and estimated relative weight of the temporal discretization error ($\mathcal{I}_t^\%$) over the kinetic energy error are reported.

Since an inviscid flow is non-dissipative and no power is introduced in Ω from the surroundings (basically, due to the imposition of periodic boundary conditions, there are no surroundings), the time evolution of the average kinetic energy over Ω quantifies the numerical dissipation introduced by the numerical scheme. In particular, we evaluate numerical dissipation based on the normalized kinetic energy error computed as follows: $(\mathcal{K}_0 - \mathcal{K}_F)/\mathcal{K}_0$, where $\mathcal{K}_0 = \int_{\Omega} \frac{1}{2} \mathbf{u}_h|_{t_0} \cdot \mathbf{u}_h|_{t_0}$ is the initial kinetic energy and $\mathcal{K}_F = \int_{\Omega} \frac{1}{2} \mathbf{u}_h|_{t_F} \cdot \mathbf{u}_h|_{t_F}$ is the final kinetic energy.

We consider $k = 1, 2, 3, 4$ HHO formulations on a h -refined regular triangular mesh sequence, the mesh cardinality reads $\text{card}(\mathcal{T}_h) = 32 \times 4^i$, $i = 0, \dots, 6$. Time integration is performed by means of a fifth-order accurate ESDIRK scheme with local time step adaptation. The trigger tolerance for time step adaptation is chosen such that the temporal error contribution weights less than 1% of the overall relative kinetic energy error. The tolerance and the estimated weight of the temporal error are reported in Table 6 for $k = 4$ HHO discretization and every grid in the mesh sequence. Clearly, the highest polynomial degree is the most demanding in terms of time integration accuracy.

In Figure 1, the relative kinetic energy error is plotted against the mesh spacing or the total number degrees of freedom (DOFs). As expected, finer meshes and higher polynomial degrees result in lower numerical dissipation. Moreover, increasing the polynomial degree systematically enhances the rate of error reduction with respect to the number of DOFs. Table 7 reports the relative kinetic energy error along with its rate of convergence for all grids and polynomial degrees combinations. We remark that the asymptotic $k + 1$ convergence rates are not fully achieved, regardless of the polynomial degree k in the HHO formulation. It is quite evident that more pronounced discrepancies are observed for higher polynomial degrees. Moreover, when the kinetic energy error is higher than 10^{-4} , the rate of error reduction does not exceed the second order, regardless of the polynomial degree. In the present numerical investigation, we were able to certify that the temporal discretization error has a negligible impact on the kinetic energy error, see Table 6. Accordingly, we wonder whether the difficulties in reaching the asymptotic convergence rates at the higher polynomial degrees indicate a lack of

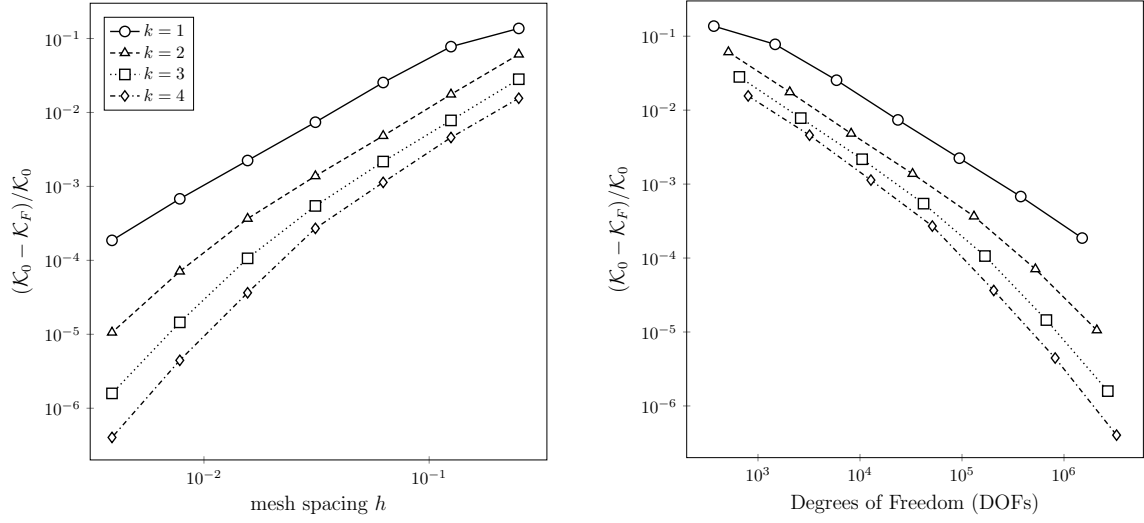


Figure 1: Double shear layer. *Left and right*, relative kinetic energy error at the end time $t_F = 2$. as a function of the mesh spacing and of the total number of degrees of freedom, respectively.

i	$\text{card}(\mathcal{T}_h)$	error ($k = 1$)	rate	error ($k = 2$)	rate	error ($k = 3$)	rate	error ($k = 4$)	rate
0	32	1.369e-01	—	6.100e-02	—	2.816e-02	—	1.557e-02	—
1	128	7.765e-02	0.82	1.755e-02	1.80	7.809e-03	1.85	4.584e-03	1.76
2	512	2.540e-02	1.61	4.828e-03	1.86	2.170e-03	1.85	1.133e-03	2.02
3	2048	7.382e-03	1.78	1.380e-03	1.81	5.444e-04	1.99	2.706e-04	2.07
4	8192	2.240e-03	1.72	3.664e-04	1.91	1.065e-04	2.35	3.644e-05	2.89
5	32768	6.792e-04	1.72	7.092e-05	2.37	1.451e-05	2.88	4.447e-06	3.03
6	131072	1.863E-04	1.87	1.059e-05	2.74	1.588E-06	3.19	4.029e-07	3.46

Table 7: Double shear layer. Numerical validation of spatial convergence of $k = 1, 2, 3, 4$ HHO formulation in terms of the kinetic energy relative error $(\mathcal{K}_0 - \mathcal{K}_F)/\mathcal{K}_0$ and corresponding rates of convergence while halving the diameter of mesh cells.

regularity of the numerical solution or whether the achievement of satisfactory asymptotic convergence rates requires finer meshes. The vorticity field depicted in Figure 2 shows that extremely high spatial accuracy is required to precisely capture the evolution of the flow field. Notice, in particular, that the two shear layers evolve into structures that are much smaller than the mesh spacing, even on the finest grid of the mesh sequence.

As an insightful indicator of the challenges involved in the double shear layer test case, the time evolution of the step size δt is shown in Figure 3. Over time, δt decreases by nearly two orders of magnitude in order to maintain the time discretization error within the prescribed tolerance. Although this variation may seem unremarkable at first glance, notice that, since we rely on a fifth order accurate time integration strategy, keeping the time step fixed might result in a tenfold increase of the temporal discretization error.

4.3 Ethier–Steinmann

In order to numerically assess the spatial convergence rates of the HHO formulation in three space dimensions, we consider the following solution of the Navier–Stokes equations proposed in [19]:

$$\begin{aligned}
u(x, y, z, t) &= -a e^{-d^2 t} (e^{ax} \sin(ay + zd) + e^{za} \cos(ax + yd)), \\
v(x, y, z, t) &= -a e^{-d^2 t} (e^{ay} \sin(az + xd) + e^{xa} \cos(ay + zd)), \\
w(x, y, z, t) &= -a e^{-d^2 t} (e^{az} \sin(ax + yd) + e^{ya} \cos(az + xd)), \\
r(x, y, z) &= 2 \sin(ax + dy) \cos(az + dx) e^{a(y+z)} + 2 \sin(ay + dz) \cos(ax + dy) e^{a(z+x)} + 2 \sin(az + dx) \cos(ay + dz) e^{a(x+y)}, \\
p(x, y, z, t) &= -\frac{a^2}{2} e^{-2d^2 t} (r(x, y, z) + e^{2ax} + e^{2ay} + e^{2az}),
\end{aligned}$$

where u , v and w are the velocity components in the x , y and z directions, respectively, p is the pressure, r is an auxiliary variable used to define the pressure and t is the time. The constant parameters are set as $a = \frac{\pi}{4}$ and $d = \frac{\pi}{2}$. We consider $\nu = \text{Re}^{-1} = 1, 0.1, 0.01$, as suggested by Ethier and Steinmann in order to avoid wiggles in the proximity of the domain boundary. The analytic solution is conceived such that the convective term is balanced by the pressure gradient and the

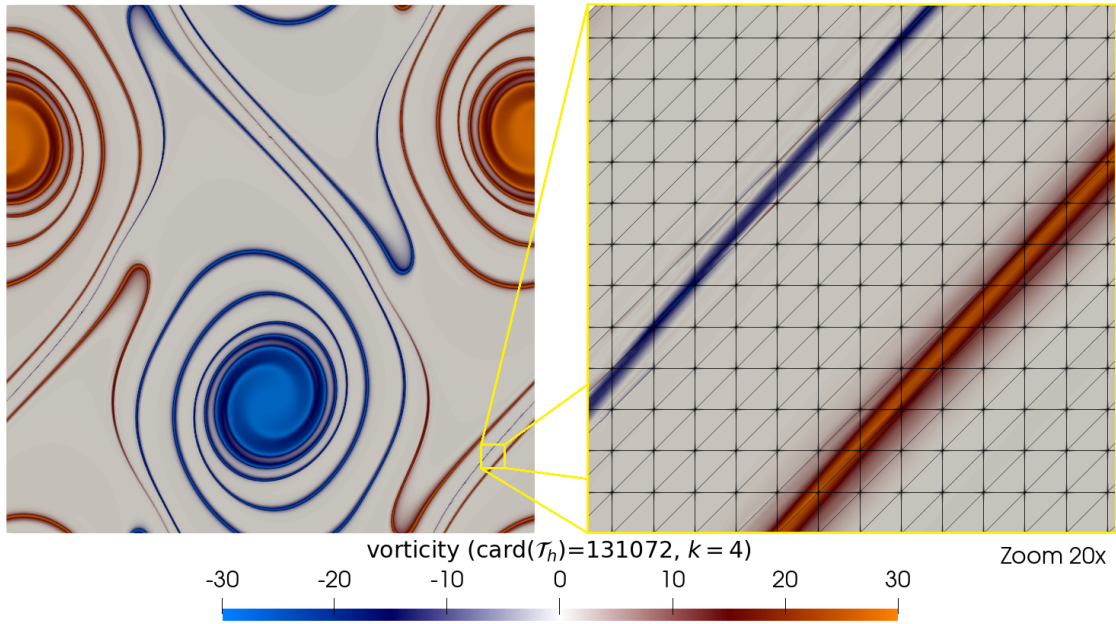


Figure 2: Double shear layer. *Left and right*: vorticity field at the end time $t = 2$ considering the whole computational domain and a zoomed-in view with the computational grid superimposed. The solution is obtained based on a $k = 4$ HHO formulation on the finest grid (left) relying on a fifth order accurate ESDIRK time marching strategy.

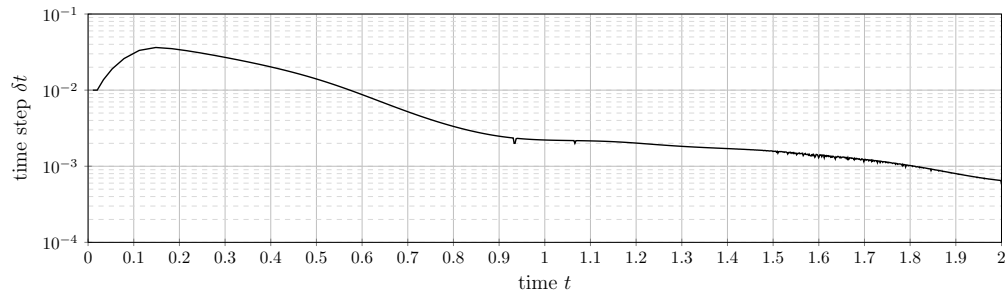


Figure 3: Double shear layer. Time step size evolution for the $k = 4$ HHO formulation over the $\text{card}(\mathcal{T}_h) = 131072$ grid.

Laplacian of the velocity is balanced by the time derivative. In order to avoid forcing terms, i.e., $\mathbf{f} = \mathbf{0}$, the velocity time derivative is multiplied by ν . The computational domain is the unit cube $\Omega = (0, 1)^3$ and time integration is carried out in the time interval $[0, 0.1]$. Accordingly the errors in L^2 norm for the velocity, the velocity gradients and the pressure are computed based on the exact solution at time $t_F = 0.1$. Dirichlet boundary conditions are enforced on five of the six faces composing $\partial\Omega$ while on the top face we impose Neumann boundary conditions. The velocity and the stress on $\partial\Omega$ are computed relying on the exact solution, the velocity field is initialized based on the exact solution.

We rely on tetrahedral meshes obtained subdividing in 24 tetrahedrons the hexahedral cells of N^3 Cartesian grids, with N cells per Cartesian direction. Accordingly, the mesh cardinality is $\text{card}(\mathcal{T}_h) = 24N^3$. The results are reported in Tables 8-9 for $k = 1, 2$ and $k = 3, 4$ HHO formulations, respectively, considering tetrahedral meshes with $N = 2i$, $i = 0, \dots, 4$. Notice that, in order to limit the computational burden, the finer meshes are avoided at the higher polynomial degrees. Time integration is performed relying on a fourth order accurate ESDIRK scheme with time step $\delta t = 0.1/160$. A $k + 1$ rate of error reduction is observed for the pressure error in L^2 norm. The velocity and velocity gradient errors in the L^2 -norm show rates of convergence of $k + 2$ and $k + 1$, respectively, in the diffusion-dominated regime, whereas the rate of error shows a tendency of being reduced by one when moving towards the convection-dominated regime.

4.4 LLMS pressure gradient test case

The LLMS pressure gradient problem is a manufactured solution for the steady incompressible Stokes equations designed by Lederer, Linke, Merdon, and Schöberl (LLMS) [28] to investigate pressure-robustness. The HHO formulation has been adapted to this test case dropping the convective term and time derivative. The analytical velocity and pressure fields read, respectively,

$$\mathbf{u} = \nabla \times \{\zeta, \zeta, \zeta\} \quad \text{and} \quad p = p_0 + x^5 + y^5 + z^5,$$

ν	$\text{card}(\mathcal{T}_h)$	$\ \nabla \mathbf{u}_h\ _{L^2(\Omega)}$	rate	$\ \mathbf{u}_h\ _{L^2(\Omega)}$	rate	$\ p_h\ _{L^2(\Omega)}$	rate	$\ \nabla \cdot \mathbf{u}_h\ _{L^2(\Omega)}$
$k = 1$								
1	24	0.1578	–	0.009606	–	0.06856	–	1.42e-15
0.1	24	0.2926	–	0.02230	–	0.05884	–	1.13e-15
0.01	24	0.8460	–	0.09202	–	0.06575	–	1.55e-15
1	192	0.04292	1.88	0.001414	2.76	0.01976	1.79	1.51e-15
0.1	192	0.1199	1.29	0.005222	2.09	0.01815	1.70	1.41e-15
0.01	192	0.2530	1.74	0.01576	2.55	0.01943	1.76	1.50e-15
1	1536	0.01134	1.92	0.0001972	2.84	0.004873	2.02	1.58e-15
0.1	1536	0.04446	1.43	0.001013	2.37	0.004583	1.99	1.57e-15
0.01	1536	0.1115	1.18	0.004127	1.93	0.005269	1.88	1.55e-15
1	12288	0.002926	1.95	2.6133e-05	2.92	0.001209	2.01	1.60e-15
0.1	12288	0.01424	1.64	0.0001641	2.63	0.001149	1.99	1.59e-15
0.01	12288	0.04806	1.21	0.001581	1.38	0.001581	1.74	1.59e-15
1	98304	0.0007440	1.98	3.3663e-06	2.96	0.0003017	2.00	1.61e-15
0.1	98304	0.004103	1.80	2.3677e-05	2.79	0.0002889	1.99	1.61e-15
0.01	98304	0.01972	1.29	0.0004833	1.71	0.0004540	1.80	1.61e-15
$k = 2$								
1	24	0.01952	–	0.0007093	–	0.01498	–	1.58e-15
0.1	24	0.03499	–	0.001655	–	0.01478	–	1.70e-15
0.01	24	0.08085	–	0.004891	–	0.01485	–	1.52e-15
1	192	0.002583	2.92	5.3018e-05	3.74	0.001511	3.31	1.71e-15
0.1	192	0.007585	2.21	0.0002083	2.99	0.001487	3.31	2.01e-15
0.01	192	0.01824	2.15	0.0008952	2.45	0.001506	3.30	1.76e-15
1	1536	0.0003383	2.93	3.6250e-06	3.87	0.0001806	3.06	1.82e-15
0.1	1536	0.001336	2.50	1.8641e-05	3.48	0.0001779	3.06	1.77e-15
0.01	1536	0.003705	2.30	9.5905e-05	3.22	0.0001814	3.05	1.84e-15
1	12288	4.3575e-05	2.96	2.3860e-07	3.93	2.2982e-05	2.97	1.83e-15
0.1	12288	0.0002090	2.68	1.4582e-06	3.68	2.2061e-05	3.01	1.81e-15
0.01	12288	0.0007603	2.29	1.2128e-05	2.98	2.2680e-05	3.00	1.78e-15

Table 8: Numerical validation of spatial convergence of $k = 1$ and $k = 2$ HHO formulations, 3D Ethier-Steinman analytical solution of the INS equations. $L^2(\Omega)$ error norms with respect to the exact solution and the corresponding rates of convergence while halving the mesh step size are reported. The temporal discretization is chosen such that the temporal approximation error is negligible, see text for details.

with arbitrary $p_0 \in \mathbb{R}$ (here set $p_0 = 1/2$) and $\zeta(x, y, z) = x^2(x-1)^2y^2(y-1)^2z^2(z-1)^2$. The forcing term \mathbf{f} within the momentum equation is set according to the analytical solution. Dirichlet boundary conditions are imposed on all but one face of the unit cubic domain $\Omega = (0, 1)^3$, while a Neumann boundary is enforced on the remaining face.

The pressure-robustness capabilities of the HHO formulation are evaluated on an h -refined sequence of meshes with cardinalities $\text{card}(\mathcal{T}_h) = 24 \times 8^i$, $i = 0, \dots, 4$, consisting of regular tetrahedral cells. Results for $k = 1, 2, 3, 4$ HHO formulations are presented in Figure 4 considering a wide range of viscosities $\nu = 10^j$, $j = -9, \dots, 3$. Given a polynomial approximation and a mesh cardinality, \mathbf{u}_h remains identical for all viscosity values. Since, while decreasing ν , the pressure error starts to dominate, this is a clear indication that velocity error is insensitive to the pressure error. This behavior clearly demonstrates the pressure-robust nature of the formulation considered. We remark that, when considering the smallest viscosity values and the highest spatial discretization accuracies, the influence of finite arithmetic precision comes into play. The velocity error grows with a factor ϵ/ν (see the dashed line in the bottom left corner of figures), where ϵ is the double-precision floating-point machine epsilon. This behavior can be explained by noticing that the Stokes problem is ill-posed in the inviscid limit, and, accordingly, it is expected that the velocity error grows unbounded approaching $\nu = 0$. In contrast, since the velocity error dominates when the viscosity is big enough, also the pressure error increases for viscosity values bigger than one.

Remark on non-simplicial meshes In this work all test cases but the ones presented in the last portion of this section consider simplicial meshes. Indeed, the theoretical analysis carried out in [9] shows that, when considering non-simplicial meshes, different choices of polynomial spaces should be adopted to maintain optimal convergence rates. In practice, as shown in Figure 5, the HHO formulation here proposed can be employed as is on prismatic and pyramidal cells maintaining pressure robustness, but losing one order of convergence for the velocity and velocity gradients error in L^2 norm. This means that the expected rate of convergences for HHO discretization of the Stokes problem on simplicial and non-simplicial meshes is $k+2$ and $k+1$, respectively, for the velocity error in L^2 -norm. The pressure error in the

ν	$\text{card}(\mathcal{T}_h)$	$\ \nabla \mathbf{u}_h\ _{L^2(\Omega)}$	rate	$\ \mathbf{u}_h\ _{L^2(\Omega)}$	rate	$\ p_h\ _{L^2(\Omega)}$	rate	$\ \nabla \cdot \mathbf{u}_h\ _{L^2(\Omega)}$
$k = 3$								
1	24	0.001746	–	5.0396E-05	–	0.001535	–	1.85E-15
0.1	24	0.003595	–	0.0001358	–	0.001514	–	1.48E-15
0.01	24	0.01563	–	0.0008673	–	0.001521	–	1.63e-15
1	192	0.0001195	3.87	1.7734e-06	4.83	9.9844e-05	3.94	1.74e-15
0.1	192	0.0003590	3.32	7.0850e-06	4.26	9.8990e-05	3.94	1.74e-15
0.01	192	0.0008174	4.26	2.0507e-05	5.40	9.9037e-05	3.94	1.65e-15
1	1536	7.8497e-06	3.93	6.0091e-08	4.88	6.2820e-06	3.99	1.70e-15
0.1	1536	3.1248e-05	3.52	3.1231e-07	4.50	6.2339e-06	3.99	1.69e-15
0.01	1536	8.8775e-05	3.20	1.2182e-06	4.07	6.2400e-06	3.99	1.71e-15
1	12288	5.0333e-07	3.96	1.9606e-09	4.94	4.1073e-07	3.93	1.70e-15
0.1	12288	2.3933e-06	3.71	1.1981e-08	4.70	3.9071e-07	4.00	1.73e-15
0.01	12288	9.2772e-06	3.26	7.9894e-08	3.93	3.9187e-07	3.99	1.72e-15
$k = 4$								
1	24	0.0001348	–	2.7618e-06	–	0.0001366	–	1.29e-15
0.1	24	0.0002599	–	7.2007e-06	–	0.0001359	–	1.30e-15
0.01	24	0.0009817	–	4.7552e-05	–	0.0001362	–	1.35e-15
1	192	4.5548e-06	4.89	5.1674e-08	5.74	4.4305e-06	4.95	1.41e-15
0.1	192	1.4792e-05	4.14	2.2006e-07	5.03	4.4080e-06	4.95	1.32e-15
0.01	192	3.4482e-05	4.83	7.3695e-07	6.01	4.4067e-06	4.95	1.33e-15
1	1536	1.5029e-07	4.92	8.8212e-10	5.87	1.8041e-07	4.62	1.42e-15
0.1	1536	6.4451e-07	4.52	4.8270e-09	5.51	1.3902e-07	4.99	1.42e-15
0.01	1536	1.8807e-06	4.20	1.8042e-08	5.35	1.3507e-07	5.03	1.39e-15

Table 9: Numerical validation of spatial convergence of $k = 3$ and $k = 4$ HHO formulations, 3D Ethier-Steinman analytical solution of the INS equations. $L^2(\Omega)$ error norms with respect to the exact solution and the corresponding rates of convergence while halving the mesh step size are reported. The temporal discretization is chosen such that the temporal approximation error is negligible, see text for details.

L^2 -norm shows a convergence rate of $k+1$ on both simplicial and non-simplicial meshes. Basically, when considering the incompressible Navier–Stokes problem on non-simplicial meshes, one can expect the same convergence rates in the viscous dominated and convection-dominated regimes.

The investigation of pressure robustness reported in Figure 5 considers $k = 2$ HHO formulations and two regular mesh sequences of cardinality $\text{card}(\mathcal{T}_h) = 6 \times 8^i$, and $\text{card}(\mathcal{T}_h) = 16 \times 8^i$, $i = 0, \dots, 4$, respectively, in case of pyramidal and prismatic mesh cells. The numerical results confirm insensitivity of the velocity field to the irrotational part of body forces.

5 Application to turbulence modelling

The extensive numerical validation conducted in the previous section suggests that the high-order accurate ESDIRK-HHO formulation should be capable of tackling incompressible flow problems in the turbulent flow regime. To this end we consider the well known Taylor–Green vortex problem at Reynolds $\text{Re} = 1\,600$. The Taylor–Green vortex problem has been widely adopted to challenge the turbulence modelling capabilities of numerical schemes [20, 21] because, despite its simple setup, proper handling of the energy cascade phenomena is required in order to precisely replicate the evolution of vortical structures. Moreover, the solver performance can be assessed comparing with DNS data available in literature. We use here the results of [38].

The computational domain is the triple periodic cube $\Omega = (-\pi, \pi)^3$ and the initial velocity and pressure fields are defined as follows:

$$\begin{aligned}
u(x, y, z) &= \sin(x) \cos(y) \cos(z), \\
v(x, y, z) &= -\cos(x) \sin(y) \cos(z), \\
w(x, y, z) &= 0, \\
p(x, y, z) &= 1 + (\cos(2x) + \cos(2y)) (\cos(2z) + 2)/16.
\end{aligned}$$

where u , v and w are the velocity components in the x , y and z directions, respectively, and p is the pressure. Time integration is performed from $t_0 = 0$ to $t_F = 20$ with $\mathbf{f} = \mathbf{0}$.

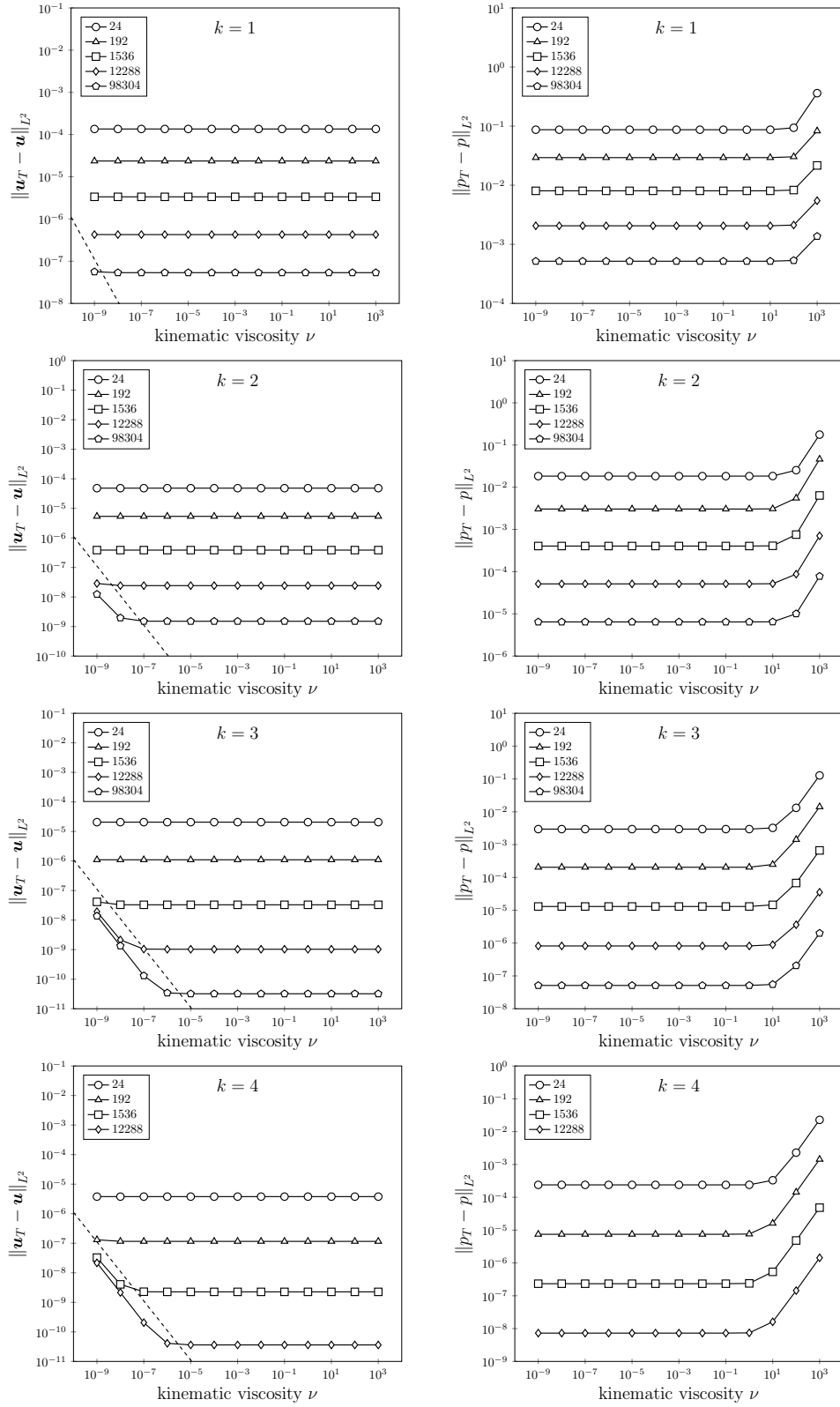


Figure 4: LLMS Stokes problem test case. *Left and right*: velocity and pressure errors varying the viscosity. We consider $k = 1, 2, 3, 4$ HHO formulations. The figure legend shows the grid cardinalities. The black dashed line depicts ϵ/ν , where $\epsilon = 1.11e - 16$ is the double-precision floating-point machine epsilon.

Since the cubic domain is periodic, all the terms written in conservative form (as the divergence of a vector field) can be eliminated from physical laws expressing conservation principles. Accordingly, the kinetic energy equation

$$\frac{d}{dt} \int_{\Omega} \frac{1}{2} \mathbf{u} \cdot \mathbf{u} = -\nu \int_{\Omega} (\nabla \times \mathbf{u}) \cdot (\nabla \times \mathbf{u}),$$

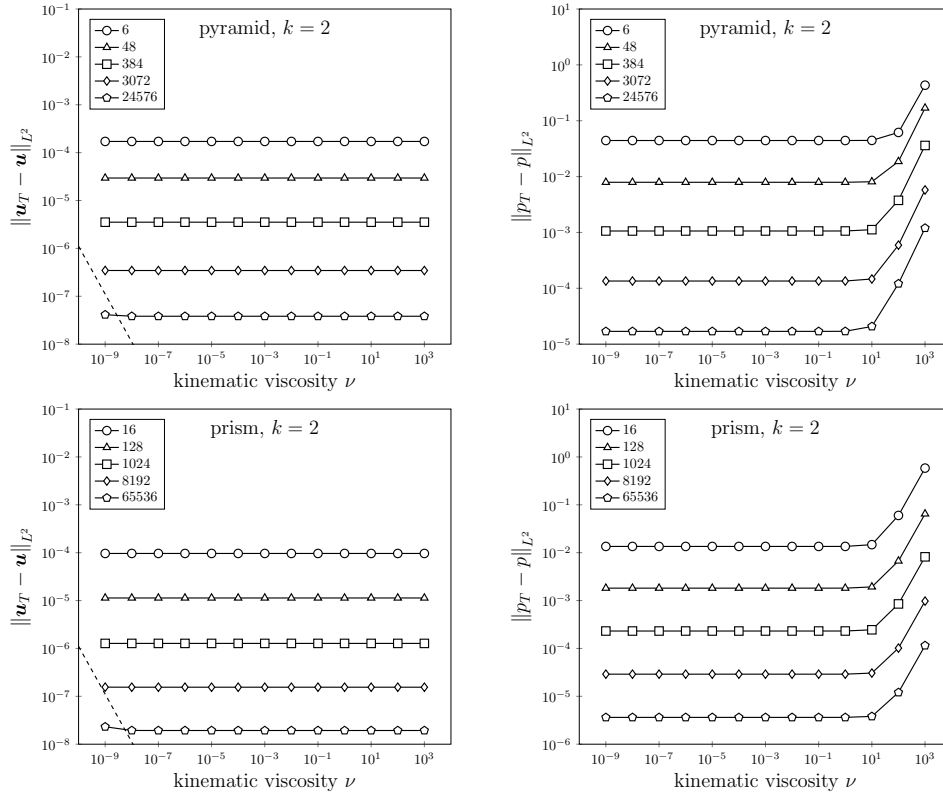


Figure 5: LLMS Stokes problem test case. *Left and right*: velocity and pressure errors in L^2 norm varying the viscosity. $k = 2$ HHO formulations on pyramidal (*top*), and prismatic (*bottom*) mesh cells are considered. The figure legend shows grid cardinalities. The black dashed line depicts ϵ/ν , where $\epsilon = 1.11 \times 10^{-16}$ is the double-precision floating-point machine epsilon.

states that time evolution of the kinetic energy is driven by the enstrophy scaled by $\nu = 1/\text{Re}$, which is the only form of energy dissipation. Accordingly, at each point in time, the most effective way of quantifying the accuracy of an approximated velocity field consist in i) comparing the average enstrophy over Ω with DNS, and ii) assessing the discrepancy, if any, between the time derivative of the average kinetic energy and the average dissipation. Clearly, the second analysis checks weather the balance of kinetic energy is properly replicated at the discrete level. Let $\mathbf{u}_h \in L^2(\Omega)^d$ be the discrete velocity solution at time t , obtained by gluing together the cell components. Introducing the physical dissipation $\mathcal{E} = \nu \int_{\Omega} (\nabla \times \mathbf{u}_h) \cdot (\nabla \times \mathbf{u}_h)$ and the total dissipation $\mathcal{E}_h = -\frac{d}{dt} \int_{\Omega} \frac{1}{2} (\mathbf{u}_h \cdot \mathbf{u}_h)$, the numerical dissipation introduced by the spatial-temporal discretization reads $\mathcal{E}_h - \mathcal{E}$.

We solve the problem on two tetrahedral elements grids: $\text{card}(\mathcal{T}_h) = 24 \times (4i)^3$, with $i = 1, 2$. The first ($i=1$) and the second ($i=2$) grid are generated starting from Cartesian meshes consisting of 4 and 8 hexahedral cells per direction, respectively, and subdividing each hexahedral cell into 24 tetrahedrons. On both those meshes, we consider ESDIRK-HHO formulations with $k = 1, \dots, 9$ and fifth order accurate time integration with local time step adaptation. On the finer grid $k = 9$, computations are missing because of lack of adequate computational resources.

In Table 10 the total number of degrees of freedom (DOF) are reported for each combination of computational grid and polynomial degree k . We distinguish among cells and faces degrees of freedom, computed as follows

$$\text{DOF}_T = \text{card}(\mathcal{T}_h) (3 \dim(\mathbb{P}_3^{k+1}) + \dim(\mathbb{P}_3^k)), \quad \text{and} \quad \text{DOF}_F = \text{card}(\mathcal{M}_h) (3 \dim(\mathbb{P}_2^k) + \dim(\mathbb{P}_2^{k+1})),$$

respectively. Notice that, thanks to static condensation, the global matrix dimension is DOF_F . Additionally, since Cartesian element meshes are commonly employed for this test case, we provide, for the sake of comparison with reference DNS data, the equivalent number of degrees of freedom per direction for each velocity component. Once again, we distinguish among cells and faces equivalent degrees of freedom, computed as follows:

$$\text{eDOFu-1D}_T = (\text{card}(\mathcal{T}_h) \dim(\mathbb{P}_3^{k+1}))^{\frac{1}{3}}, \quad \text{and} \quad \text{eDOFu-1D}_F = (\text{card}(\mathcal{M}_h) \dim(\mathbb{P}_2^k))^{\frac{1}{3}},$$

respectively. DNS data is obtained based on a spatial resolution of 512 degrees of freedom per Cartesian direction for each velocity component.

The user-defined threshold tolerance for tuning the local time step adaptation procedure and the corresponding total number of time steps ($N_{\delta t}$) are reported in Table 11. The minimum and maximum time steps encountered along the

grid 24×4^3					grid 24×8^3				
k	DOF _T	DOF _F	eDOFu-1D _T	eDOFu-1D _F	k	DOF _T	DOF _F	eDOFu-1D _T	eDOFu-1D _F
1	15360	9216	25	21	1	405504	368640	50	42
2	30720	18432	31	26	2	847872	688128	63	53
3	53760	30720	38	31	3	1523712	1105920	75	63
4	86016	46080	44	36	4	2482176	1622016	88	72
5	129024	64512	51	40	5	3772416	2236416	101	80
6	184320	86016	57	44	6	5443584	2949120	114	88
7	253440	110592	63	48	7	7544832	3760128	127	96
8	337920	138240	70	52	8	10125312	4669440	139	103
9	439296	168960	76	55					

Table 10: Taylor–Green vortex test case. Total number of cells (DOF_T) and faces (DOF_F) degrees of freedom. For the sake of comparison with DNS data and other methods employing Cartesian element meshes we also provide the equivalent number of degrees of freedom per direction for each velocity component. We distinguish among cells (eDOFu-1D_T) and faces (eDOFu-1D_F) equivalent DOFs.

grid 24×4^3					grid 24×8^3				
k	tol_a	$N_{\delta t}$	δt_{MIN}	δt_{MAX}	k	tol_a	$N_{\delta t}$	δt_{MIN}	δt_{MAX}
1	1e-04	24	4.91e-1	1.50e-0	1	1e-04	39	3.68e-1	7.77e-1
2	1e-04	34	4.14e-1	1.05e-0	2	1e-05	111	9.51e-2	5.44e-1
3	1e-04	45	2.84e-1	1.12e-0	3	1e-05	133	6.90e-2	7.56e-1
4	1e-04	56	1.67e-1	1.00e-0	4	1e-05	155	5.55e-2	7.46e-1
5	1e-04	69	1.35e-1	8.44e-1	5	1e-05	168	4.72e-2	7.46e-1
6	1e-04	78	1.14e-1	9.69e-1	6	1e-05	180	3.99e-2	7.46e-1
7	1e-04	86	9.67e-2	9.68e-1	7	1e-05	193	4.32e-2	7.46e-1
8	3.16e-05	120	6.35e-2	8.23e-1	8	1e-05	204	4.19e-2	6.01e-1
9	1e-05	172	4.22e-2	7.46e-1					

Table 11: Taylor–Green vortex test case, ESDIRK-HHO formulation with fifth order accuracy in time. User-defined adaptation trigger tolerance (tol_a), total number of time steps ($N_{\delta t}$), minimum (δt_{MIN}) and maximum step size (δt_{MAX}) are reported for each combination of computational grid and polynomial degree k .

time integration history are also tabulated, and the minimum step size is more than an order of magnitude smaller than the maximum. Thanks to the combination of fully implicit time integration and local time step adaptation, the number of time steps required to complete the simulation is relatively small. It is possible to appreciate that increasing the polynomial degree of the HHO discretization leads to an increased number of time steps, even if the threshold tolerance is kept fixed. This behavior can be motivated considering that the timescales of smaller vortical structures are smaller and that increasing the spatial accuracy allows to resolve higher-and-higher wavenumbers. We can indeed confirm that the time integration marches with the smaller time steps right after the peak of dissipation. The steep rise of the number of time steps suggests that, for the chosen value of tol_a , the temporal error is still negligible compared to the spatial error and does not limit the overall accuracy.

In Figure 6, besides comparing the relative enstrophy $\frac{\mathcal{E}}{\mathcal{E}_0}$ with DNS data, we show the relative total dissipation $\frac{\mathcal{E}_h}{\mathcal{E}_{h0}}$ and the relative numerical dissipation $\frac{\mathcal{E}_h - \mathcal{E}}{\mathcal{E}_0}$ for a subset of the runs. We simply consider the most relevant results, that is the most accurate ones, in order to show the influence of refining the grid and increasing the polynomial degree. Notice that, for sake of conciseness, the notation $\mathcal{E}_0 = \mathcal{E}|_{t_0}$ and $\mathcal{E}_{h0} = \mathcal{E}_h|_{t_0}$ is employed. We remark that, when considering relative quantities (with respect to initial time $t = 0$), we can alternatively refer to enstrophy or dissipation, and, in case of DNS, total and physical dissipation are basically the same. As reported in the literature, the enstrophy behavior is the most challenging to replicate. The relative total dissipation shows good agreement with the DNS relative enstrophy, even at relatively low polynomial degrees, confirming the robustness of the ESDIRK-HHO formulation in under resolved computations. However, we remark that, on the coarser grid, the total dissipation curve is shifted to the left compared to DNS data, even at the highest $k = 9$ polynomial degree. Note that, in the enstrophy increasing phase, $k = 7, 8, 9$ computations are in good agreement in terms of total dissipation, suggesting that much higher polynomial degrees would be required to properly replicate DNS. The behaviour of the numerical dissipation outlines the benefit of increasing the polynomial degree and refining the grid. We remark that, on the finer grid at $k = 8$, the maximum relative numerical dissipation is smaller than one, which, compared with the relative enstrophy value at peak, implies that the evolution of kinetic energy shows a 3% discrepancy with respect to a fully resolved computation.

In Figure 7 we compare the relative kinetic energy $\mathcal{K}/\mathcal{K}_0$ time evolution with DNS data for the most accurate results on each mesh. Notice that $\mathcal{K}_0 = \mathcal{K}|_{t_0}$. On the coarser grid, the left shift of the dissipation observed in the entropy analysis induces an earlier than expected decrease of the kinetic energy. On the finer grid, the evolution of kinetic energy

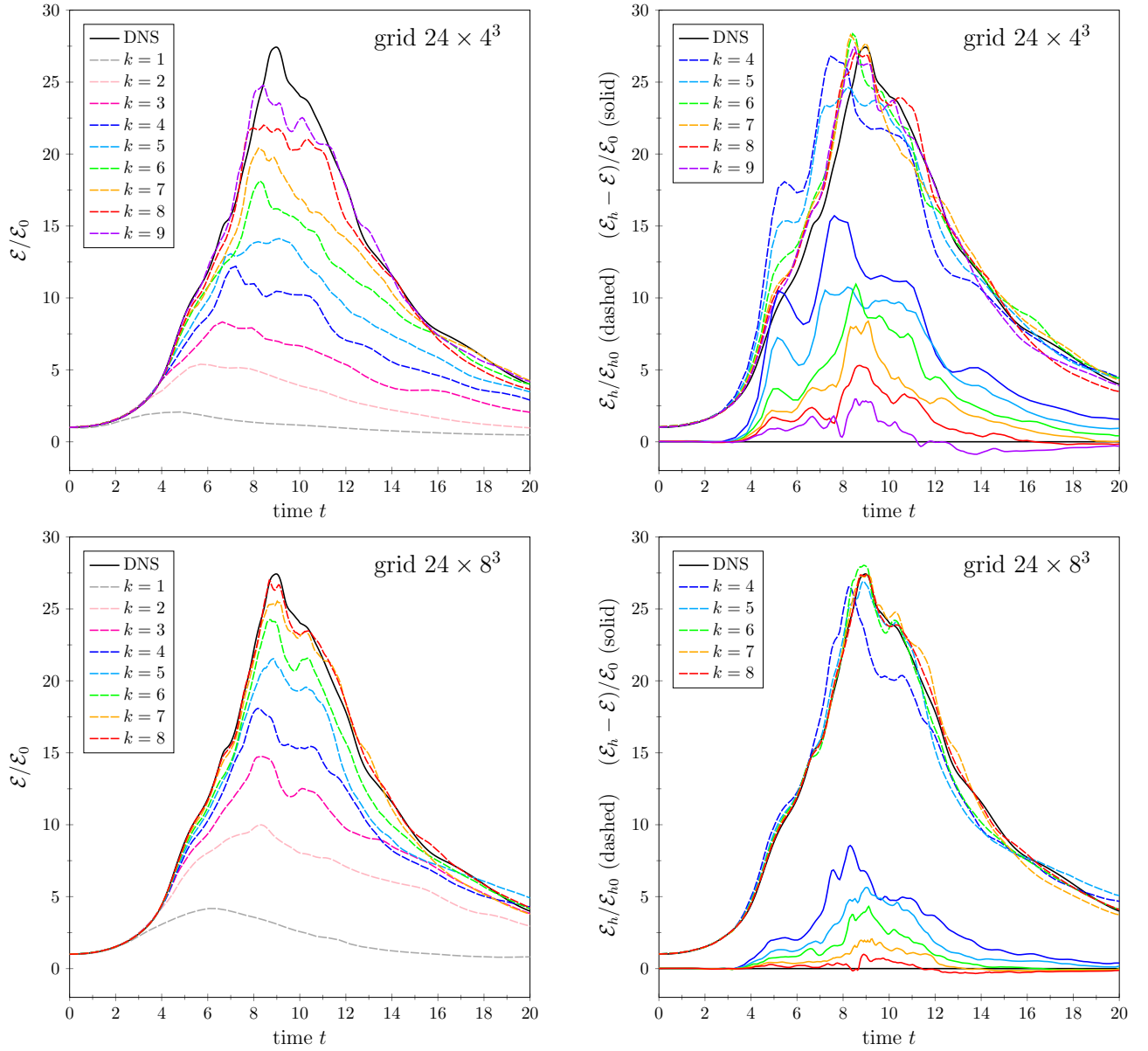


Figure 6: Taylor–Green vortex test case, ESDIRK-HHO formulation with fifth order accuracy in time and $k = 1, \dots, 9$. Adaptive local time stepping is employed. *Left*: relative enstrophy $\frac{\mathcal{E}}{\mathcal{E}_0}$ (dashed line). *Right*: Relative total dissipation $\frac{\mathcal{E}_h}{\mathcal{E}_{h0}}$ (dotted line) and relative numerical dissipation $\frac{\mathcal{E}_h - \mathcal{E}}{\mathcal{E}_0}$ (solid line), see text for details. The notation $\mathcal{E}_0 = \mathcal{E}|_{t_0}$ and $\mathcal{E}_{h0} = \mathcal{E}_h|_{t_0}$ is employed.

replicates DNS data in the entropy increasing phase while some discrepancies can still be appreciated in the entropy decreasing phase. Nevertheless, the improvements gained increasing the polynomial degree suggests that a full resolution of energy cascade phenomena is not out of reach.

Overall, considering that the computational meshes are rather coarse and unstructured, which is probably suboptimal for this test case, the results are satisfactory. Note that, despite the number of degrees of freedom is a fraction of the amount employed to achieve DNS data, the trend towards DNS is confirmed by increasingly precise replication of the enstrophy behavior. We remark that the focus on tetrahedral elements meshes is motivated by the observation that four nodes tetrahedral cells have planar faces, independently of the disposition of the nodes. We also remind that planar faces are essential to retain efficiency of static condensation and pressure robustness all together [6, 39]. Accordingly, when tackling complex computational domains, relying on simplicial meshes is a viable and straightforward choice in the context of hybrid formulations. We also refer to Section 4.4 for a discussion on the application of ESDIRK-HHO to non-simplicial meshes.

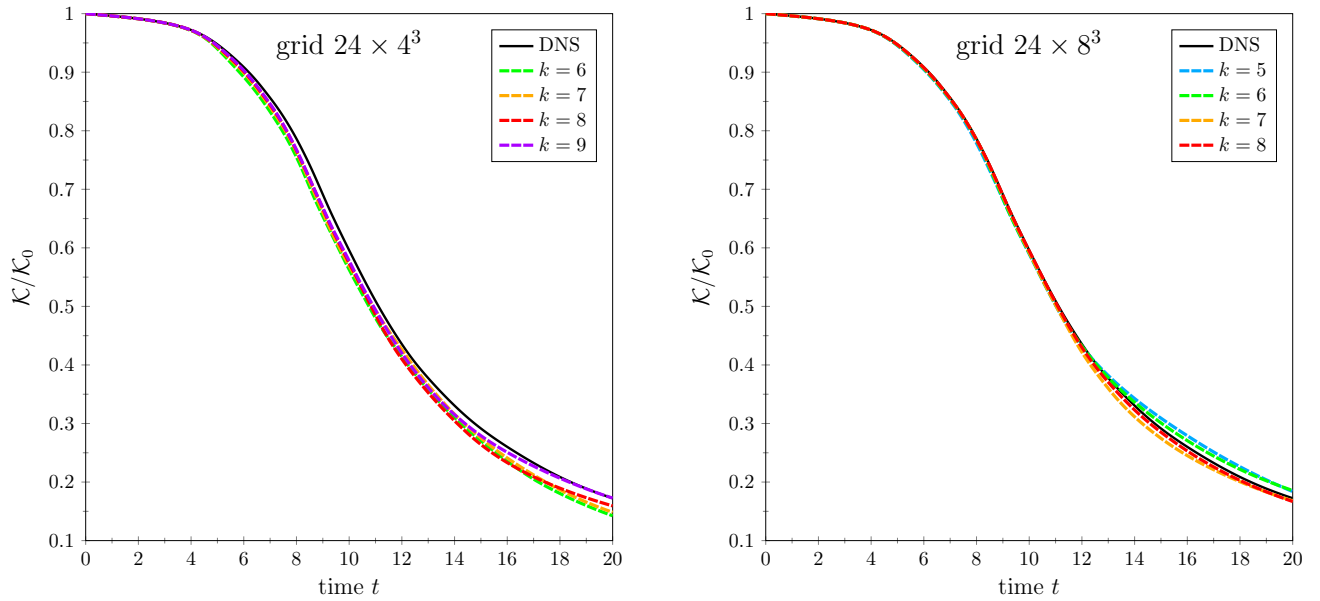


Figure 7: Taylor–Green vortex test case, ESDIRK-HHO formulation with fifth order accuracy in time. Adaptive local time stepping is employed. *Left and right*: relative kinetic energy evolution $\frac{K}{K_0}$ on the coarse 24×4^3 and the fine 24×8^3 grids. The notation $K_0 = K|_{t_0}$ is employed.

6 Conclusion

We provided extensive numerical validation, in both two and three space dimensions, of an ESDIRK-HHO formulation of the incompressible Navier–Stokes equations that is capable of reaching high-orders of accuracy in both space and time. Relevant features are pressure-robustness, that is decoupling of the velocity error with respect to the pressure error, and exact conservation of mass, with point-wise divergence free velocity fields. The proposed implementation relies on p -multilevel solution strategies and static condensation to alleviate the computational burden associated with fully implicit time marching strategies. This combination has proved effective thanks to use of fully hybrid polynomial spaces, for both the velocity and the pressure. Moreover, the time step can be locally adapted to improve accuracy of the time integration.

Robustness has been demonstrated tackling challenging test case and considering both viscous dominated and convection-dominated flow regimes, up to the inviscid limit. To corroborate the turbulence modelling capabilities claim, we performed the Taylor–Green Vortex problem showing the ability to reach DNS like precision in the relevant flow features measures employing coarse meshes and high-polynomial degrees.

Acknowledgements

Daniele Di Pietro acknowledges funding by the European Union (ERC Synergy, NEMESIS, project number 101115663). Views and opinions expressed are however those of the authors only and do not necessarily reflect those of the European Union or the European Research Council Executive Agency. Neither the European Union nor the granting authority can be held responsible for them.

References

- [1] J. Aghili, S. Boyaval, and D. A. Di Pietro. Hybridization of mixed high-order methods on general meshes and application to the Stokes equations. *Comput. Meth. Appl. Mat.*, 15(2):111–134, 2015.
- [2] Satish Balay, Shrirang Abhyankar, Mark F. Adams, Jed Brown, Peter Brune, Kris Buschelman, Lisandro Dalcin, Victor Eijkhout, William D. Gropp, Dinesh Kaushik, Matthew G. Knepley, Lois Curfman McInnes, Karl Rupp, Barry F. Smith, Stefano Zampini, and Hong Zhang. PETSc users manual. Technical Report ANL-95/11 - Revision 3.6, Argonne National Laboratory, 2015.
- [3] F. Bassi, L. Botti, A. Colombo, D. A. Di Pietro, and P. Tesini. On the flexibility of agglomeration based physical space discontinuous Galerkin discretizations. *J. Comput. Phys.*, 231(1):45–65, 2012.
- [4] L. Beirão da Veiga, D. A. Di Pietro, J. Droniou, K. B. Haile, and T. J. Radley. A Reynolds-semi-robust method with hybrid velocity and pressure for the unsteady incompressible Navier–Stokes equations, 2 2025.

- [5] John B. Bell, Phillip Colella, and Harland M. Glaz. A Second-Order Projection Method for the Incompressible Navier–Stokes Equations. *J. Comput. Phys.*, 85:257–283, 1989.
- [6] L. Botti and D. A. Di Pietro. Numerical assessment of Hybrid High-Order methods on curved meshes and comparison with discontinuous Galerkin methods. *J. Comput. Phys.*, 370:58–84, 2018.
- [7] L. Botti and D. A. Di Pietro. p -multilevel preconditioners for hho discretizations of the Stokes equations with static condensation. *Commun. Appl. Math. Comput.*, 4(3):783–822, 2022.
- [8] L. Botti, D. A. Di Pietro, and J. Droniou. A Hybrid High-Order method for the incompressible Navier–Stokes equations based on Temam’s device. *J. Comput. Phys.*, 376:786–816, 2019.
- [9] Lorenzo Botti, Michele Botti, Daniele A. Di Pietro, and Francesco Carlo Massa. Stability, convergence, and pressure-robustness of numerical schemes for incompressible flows with hybrid velocity and pressure. *Math. Comp.*, 01 2025.
- [10] Lorenzo Botti and Francesco Carlo Massa. Hho methods for the incompressible navier-stokes and the incompressible euler equations. *Journal of Scientific Computing*, 92(28):397–434, 06 2022.
- [11] Lorenzo Botti and Daniele A. Di Pietro. p-Multilevel Preconditioners for HHO Discretizations of the Stokes Equations with Static Condensation. *Commun. Appl. Math. Comput.*, 4:783–822, 2022.
- [12] Daniel Castanon Quiroz and Daniele A. Di Pietro. A hybrid high-order method for the incompressible navier–stokes problem robust for large irrotational body forces. *Computers & Mathematics with Applications*, 79(9):2655–2677, 2020.
- [13] Daniel Castanon Quiroz and Daniele A Di Pietro. A pressure-robust hho method for the solution of the incompressible navier–stokes equations on general meshes. *IMA Journal of Numerical Analysis*, 44(1):397–434, 04 2023.
- [14] B. Cockburn, D. A. Di Pietro, and A. Ern. Bridging the Hybrid High-Order and Hybridizable Discontinuous Galerkin methods. *ESAIM: M2AN*, 50(3):635–650, 2016.
- [15] D. A. Di Pietro and J. Droniou. *The Hybrid High-Order method for polytopal meshes*. Number 19 in Modeling, Simulation and Application. Springer, Cham, 2020.
- [16] D. A. Di Pietro, J. Droniou, and A. Ern. A discontinuous-skeletal method for advection-diffusion-reaction on general meshes. *SIAM J. Numer. Anal.*, 53(5):2135–2157, 2015.
- [17] D. A. Di Pietro, A. Ern, A. Linke, and F. Schieweck. A discontinuous skeletal method for the viscosity-dependent Stokes problem. *Comput. Meth. Appl. Mech. Engrg.*, 306:175–195, 2016.
- [18] D. A. Di Pietro and S. Krell. A Hybrid High-Order method for the steady incompressible Navier–Stokes problem. *J. Sci. Comput.*, 74(3):1677–1705, 2018.
- [19] C. Ross Ethier and D. A. Steinman. Exact fully 3d navier–stokes solutions for benchmarking. *International Journal for Numerical Methods in Fluids*, 19(5):369–375, 1994.
- [20] Niklas Fehn, Martin Kronbichler, Christoph Lehrenfeld, Gert Lube, and Philipp W. Schroeder. High-order dg solvers for underresolved turbulent incompressible flows: A comparison of l2 and h(div) methods. *International Journal for Numerical Methods in Fluids*, 91(11):533–556, 2019.
- [21] Niklas Fehn, Wolfgang A. Wall, and Martin Kronbichler. Robust and efficient discontinuous galerkin methods for under-resolved turbulent incompressible flows. *Journal of Computational Physics*, 372:667–693, 2018.
- [22] Antonio Ghidoni, Francesco Carlo Massa, Gianmaria Noventa, and Stefano Rebay. Assessment of an adaptive time integration strategy for a high-order discretization of the unsteady RANS equations. *International Journal for Numerical Methods in Fluids*, 94(12):1923–1963, 2022.
- [23] Ernst Hairer and Gerhard Wanner. *Solving Ordinary Differential Equations II*. Springer Series in Computational Mathematics, 1996.
- [24] Christopher A. Kennedy and Mark H. Carpenter. Additive runge–kutta schemes for convection–diffusion–reaction equations. *Applied Numerical Mathematics*, 44(1):139–181, 2003.
- [25] Christopher A. Kennedy and Mark H. Carpenter. Diagonally Implicit Runge-Kutta Methods for Ordinary Differential Equations. A Review. Technical Report NASA/TM-2016-219173, NASA Langley Research Center, 2016.
- [26] Keegan L. A. Kirk and Sander Rhebergen. Analysis of a Pressure-Robust Hybridized Discontinuous Galerkin Method for the Stationary Navier–Stokes Equations. *J. Sci. Comput.*, 81(2):881–897, 11 2019.

- [27] J. Lang and D. Teleaga. Towards a fully space-time adaptive FEM for magnetoquasistatics. *Magnetics, IEEE Transactions on*, 44(6):1238–1241, June 2008.
- [28] Philip L. Lederer, Alexander Linke, Christian Merton, and Joachim Schöberl. Divergence-free Reconstruction Operators for Pressure-Robust Stokes Discretizations with Continuous Pressure Finite Elements. *SIAM J. Numer. Anal.*, 55(3):1291–1314, 2017.
- [29] Christoph Lehrenfeld and Joachim Schöberl. High order exactly divergence-free hybrid discontinuous galerkin methods for unsteady incompressible flows. *Computer Methods in Applied Mechanics and Engineering*, 307:339–361, 2016.
- [30] Alexander Linke. On the role of the Helmholtz decomposition in mixed methods for incompressible flows and a new variational crime. *Comput. Methods Appl. Mech. Engrg.*, 268:782–800, 2014.
- [31] G. Noventa, F. Massa, S. Rebay, F. Bassi, and A. Ghidoni. Robustness and efficiency of an implicit time-adaptive discontinuous galerkin solver for unsteady flows. *Computers & Fluids*, 204:104529, 2020.
- [32] Weifeng Qiu and Lina Zhao. $H(\text{div})$ -conforming HDG methods for the stress-velocity formulation of the Stokes equations and the Navier–Stokes equations. *Numerische Mathematik*, 156:1639–1678, 2024.
- [33] Daniel Castanon Quiroz and Daniele A. Di Pietro. A reynolds-semi-robust and pressure-robust hybrid high-order method for the time dependent incompressible navier–stokes equations on general meshes. *Computer Methods in Applied Mechanics and Engineering*, 436:117660, 2025.
- [34] Sander Rhebergen and Garth N. Wells. A hybridizable discontinuous Galerkin method for the Navier-Stokes equations with pointwise divergence-free velocity field. *J. Sci. Comput.*, 76(3):1484–1501, 2018.
- [35] Gustaf Soderlind. Digital filters in adaptive time-stepping. *ACM Trans. Math. Softw.*, 29(1):1–26, March 2003.
- [36] Gustaf Soderlind and Lina Wang. Adaptive time-stepping and computational stability. *Journal of Computational and Applied Mathematics*, 185(2):225 – 243, 2006. Special Issue: International Workshop on the Technological Aspects of Mathematics.
- [37] Geoffrey Ingram Taylor and Albert Edward Green. Mechanism of the production of small eddies from large ones. *Proceedings of the Royal Society of London. Series A - Mathematical and Physical Sciences*, 158(895):499–521, 1937.
- [38] Wim M. van Rees, Anthony Leonard, D.I. Pullin, and Petros Koumoutsakos. A comparison of vortex and pseudo-spectral methods for the simulation of periodic vortical flows at high reynolds numbers. *Journal of Computational Physics*, 230(8):2794–2805, 2011.
- [39] Liam Yemm. A new approach to handle curved meshes in the Hybrid High-Order method. *Foundations of Computational Mathematics*, 24:1049–1076, 2024.